



**School of Mechanical and Manufacturing Engineering**

**Faculty of Engineering**

**UNSW Sydney**

BY

**Sophie Schiffmann**

**An Investigation into the Effectiveness of Vortex Generator Cooling on  
Photovoltaic Modules under Forced Convection Conditions**

A Thesis submitted as a requirement for the degree of Bachelor of Engineering in Mechanical  
Engineering

Submitted: 17.11.2023

Student zID: z5308411

Supervisor: Dr Charitha de Silva (UNSW)

## **ORIGINALITY STATEMENT**

I, Sophie Schiffmann, hereby declare that this submission is my own work and to the best of my knowledge it contains no materials previously published or written by another person, or substantial proportions of material which have been accepted for the award of any other degree or diploma at UNSW or any other educational institution, except where due acknowledgement is made in the thesis. Any contribution made to the research by others, with whom I have worked at UNSW or elsewhere, is explicitly acknowledged in the thesis. I also declare that the intellectual content of this thesis is the product of my own work, except to the extent that assistance from others in the project's design and conception or in style, presentation and linguistic expression is acknowledged.

Signed



Date 17.11.2023

## **Abstract**

PV modules currently experience issues pertaining to longevity and electrical output through the incident formation of thermal energy by operating under the Sun. Promoting cooling to modules presents a novel way in combatting the limitations of solar energy. This thesis has sought to achieve this by experimentally assessing the effect of rectangular vortex generators (VGs) on the roofing layer (so as to not infringe on module warranty conditions) to enhance the convection heat flux on the module's rear surface. To realistically situate the experiment, the cooling capabilities of VGs were evaluated under the presence of forced convection, using a large wind tunnel to simulate wind speed of 1m/s, 2m/s and 3m/s. The results indicated a blend of full, forward and backwards facing VGs produced the best cooling potential of 1.82°C, relating to roughly a 15% increase in module lifespan. All but one of the cases assessed presented cooling to some degree. The significance of these findings lies in the potential to reduce PV module waste and enhance power returns, contributing to the sustainability and efficiency of solar energy systems.

## **Acknowledgements**

I'd like to thank my supervisor Dr Charitha de Silva for his guidance and help to increase my learning in this field. Thank you to the remainder of the team of this project for their insights and contributions to the CFD side of this project, particularly to Svetlana Tkachenko. I am deeply grateful to Tingyi Zhang who has been a constant source of support and has been available throughout the whole year to help run the experiments, assist in processing and produce high quality results. I would not have been able to do this thesis without him.

Shoutout to my parents, family and friends for being legends.

# Contents

Abstract.....	iii
Acknowledgements.....	iv
List of figures.....	vii
List of tables.....	ix
Nomenclature.....	x
1. Introduction.....	1
2. Literature review.....	2
2.1 Genealogy and Limitations.....	2
2.2 Heat Transfer and PV Modules.....	5
2.3 Convective Cooling.....	6
2.4 Convective Cooling Methods.....	9
2.4.1 Passive Cooling Methods.....	9
2.4.2 Active Cooling Methods.....	10
2.4.3 Vortex generators.....	12
2.5 Experimental Measurement Techniques.....	16
2.5.1 Computational Fluid Dynamics.....	16
2.5.2 Infrared Thermography.....	16
3 Methodology.....	18
3.1 Motivations and Aims.....	18
3.2 Overview of Experimentation.....	19
3.3 Experimental Equipment.....	20
3.4 Experimentation.....	23
3.4.1 PV Module Configuration.....	23
3.4.2 Data Acquisition.....	25
3.4.3 Environmental Conditions and Assumptions.....	26
3.5 Data Processing.....	26
3.5.1 FLIR Processing.....	26
3.5.2 MATLAB Processing.....	28
4 Results and Discussion.....	29
4.1 Characterisation of the Wind Tunnel and Ambient Temperature Considerations.....	29
4.2 Baseline Results and Temperature Fits.....	31
4.3 VG Results.....	33
4.3.1 Thermal Behaviour Analysis.....	34
4.4 Experimental against Simulation.....	38
4.5 Design Modifications to Experimental Frame.....	39
5 Conclusions and Future Work.....	42
References.....	44
Appendices.....	52

Appendix A ..... 52

Appendix B ..... 53

Appendix C ..... 54

Appendix D ..... 55

Appendix E ..... 62

## List of figures

Figure 1 Electrical efficiency as a function of PV temperature [20] .....	3
Figure 2 Electricity process through p-type (left) and n-type semiconductors [22] .....	3
Figure 3 Impact of temperature on current and voltage of a solar cell [23].....	4
Figure 4 Heat distribution over world [35] .....	5
Figure 5 Heat transfer schematic for PV module.....	5
Figure 6 Boundary layers formed from flow (left) and convection flows over inclined plate (right) [38]...	7
Figure 7 Relative temperatures from leading edge for varying inclines [43] .....	8
Figure 8 Variation of CHTC with Reynolds number on a flat plate [38] .....	9
Figure 9 Various airflow channel configurations [59] .....	12
Figure 10 Vortex generator shapes [66].....	13
Figure 11 Attack angle against efficiency [70] .....	14
Figure 12 Reynolds number against heat transfer enhancement and rows of VGs [70].....	15
Figure 13 Temperature profiles at the middle plane of the cooling channel [72] .....	15
Figure 14 A comparison between theoretical and experimental results. [20] .....	16
Figure 15 Velocimeter .....	21
Figure 16 Thermocouple placements across PV module configuration .....	22
Figure 17 Experimental set up using IR camera .....	23
Figure 18 LTS with PV frame inside (isometric view, left) (side view, right) .....	23
Figure 19 Wind direction and spacing dimensions .....	24
Figure 20 fwd_half formation      Figure 21 fwd_full formation .....	24
Figure 22 back_half formation      Figure 23 back_full formation.....	24
Figure 24 fwdback_full formation .....	25
Figure 25 Top view of side panel boundary layers      Figure 26 Side view of PV module and acrylic base boundary layers .....	25
Figure 27 Images taken by FLIR camera; left – normal, right – IR image.....	27
Figure 28 Box method processing .....	28
Figure 29 Region of interest zone .....	29
Figure 30 Relative temperature changes of LWT system .....	30
Figure 31 Temperature changes of LWT against different wind speeds .....	31
Figure 32 Fitline trends using average surface temperatures .....	31
Figure 33 8 row trendlines for 1m/s      Figure 34 8 row trendlines for 2m/s .....	32
Figure 35 8 row trendlines for 3m/s.....	32
Figure 36 Temperature trend across PV      Figure 37 Temperature trend across PV.....	33

Figure 38 Temperature trend across PV module rows for 3m/s .....	33
Figure 39 Delta T between baseline and VG case graphically .....	34
Figure 40 Delta T trend for rows 1:8      Figure 41 Delta T trend for rows 2:8 .....	34
Figure 42 fwd_full Delta T trend      Figure 43 fwd_half Delta T trend .....	35
Figure 44 back_full Delta T trend      Figure 45 back_half Delta T trend .....	35
Figure 46 fwdback_full Delta T trend.....	35
Figure 47 Vortex creation against forward facing VG; left – diagram, right – CFD.....	37
Figure 48 Vortex creation against backwards facing VG; left – diagram, right – CFD .....	37
Figure 49 Example of future formations to assess .....	38
Figure 50 fwd_full Delta T comparison      Figure 51 fwd_half Delta T comparison .....	39
Figure 52 back_full Delta T comparison      Figure 53 back_half Delta T comparison.....	39
Figure 54 Photo of misaligned VGs and collapsed array .....	40
Figure 55 Designs to hold VGs in place; left - rungs, right - L-shapes .....	40
Figure 56 Cooling effect wooden board produce compared to the acrylic baselines.....	41



**List of tables**

Table 1 Properties of PV module..... 20

Table 2 Fitline equations for each speed..... 32

## Nomenclature

$\beta$	<i>Attack angle of vortex generator</i>
$\delta$	<i>Boundary layer thickness</i>
$\Delta T$	<i>Experimental Temperature Difference</i>
$\varepsilon$	<i>Emissivity</i>
$\eta$	<i>Efficiency</i>
$\theta$	<i>Incline of PV module</i>
$\tau$	<i>Transmission</i>
$A$	<i>Current</i>
<i>BIPV</i>	<i>Building-Integrated Photovoltaics</i>
<i>CAD</i>	<i>Computer Aided Design</i>
<i>CFD</i>	<i>Computational Fluid Dynamics</i>
<i>CHTC</i>	<i>Convective heat transfer coefficient</i>
$G$	<i>Roof spacing / Channel gap</i>
$G_n$	<i>Solar irradiance</i>
$H$	<i>Height of vortex generator</i>
<i>IR</i>	<i>Infrared</i>
$L$	<i>Length of vortex generator</i>
<i>LTS</i>	<i>Large Test Section</i>
<i>LWT</i>	<i>Large Wind Tunnel</i>
$Q_{cd}$	<i>Heat transfer via conduction</i>
$Q_{cv}$	<i>Heat transfer via convection</i>
$Q_r$	<i>Heat transfer via radiation</i>
<i>RANS</i>	<i>Reynolds-Averaged Navier-Stokes</i>
<i>PIV</i>	<i>Particle Image Velocimetry</i>
<i>PV</i>	<i>Photovoltaic</i>
$P_{in}$	<i>Power in</i>
$P_{out}$	<i>Power out</i>
$P_x$	<i>Horizontal (spanwise) spacing</i>
$P_y$	<i>Vertical (streamwise) spacing</i>
$Re$	<i>Reynolds Number</i>
$T$	<i>Temperature</i>
<i>TMS</i>	<i>Thin metal sheet</i>

$T_{ambient}$	<i>Ambient temperature</i>
$T_{module}$	<i>Module temperature</i>
$T_{roof,top}$	<i>Temperature on the upper roof</i>
$T_{roof,bottom}$	<i>Temperature on the lower roof</i>
$T_{entrance}$	<i>Temperatures of inlet air of the gap channel</i>
$T_{exit}$	<i>Temperatures of outlet air of the gap channel</i>
$V$	<i>Velocity</i>
$V$	<i>Voltage</i>
$VG$	<i>Vortex generator</i>
$V_{OC}$	<i>Open circuit voltage</i>
$W$	<i>Width of vortex generator</i>
$W_{ambient}$	<i>Ambient radiation</i>
$W_{atmospheric}$	<i>Atmospheric radiation</i>
$W_{body}$	<i>Body radiation</i>
$W_{tot}$	<i>Total radiation power</i>

# 1. Introduction

An imperative need for renewable energy to dominate the energy sector has been driven by two pivotal events; the exponential production of greenhouse emissions over the last century has intensified climate events and exacerbated environmental degradation, and Russia's invasion of Ukraine early 2022 forcing an energy crisis globally [1], [2]. With 84.3% of global populations sourcing electricity from fossil fuels (due to the resource being rich in energy and relatively cheap to source and produce) energy independence is necessary in upcoming years to combat the effects of climate change and provide cost effective energy that is sustainable in the long term [3].

Fortunately, solar energy is globally abundant and inexhaustible in supply. Every second, the Earth receives 10,000 times the amount of energy the entire globe uses as solar radiation, that is, 173,000 terawatts [4]. Despite the prevalence of solar energy, some 775 million people (mostly situated to Africa) do not have access to electricity, and current commercial solar infrastructure technology is constrained by efficiency conversion capabilities to approximately 15-20%, which ultimately declines with years of use [5], [6]. In regions which experience ample global irradiation, efficiency is further eroded by 0.4-0.65% for every degree increase in temperature beyond designed limits as a result of excessive amounts of thermal energy [7]. These limitations in PV module efficiency reduces the working lifespan and potential power output, underpinning a stunted exponential uptake in solar technologies worldwide [8].

The latest energy economic climate and societal positioning on climate change has given leverage for this energy transition to occur. Solar energy currently accounts for 0.1% of Australia's total primary energy consumption, and only a third of households currently have rooftop PV modules installed [9], [10]. Latest forecasts have predicted global solar PV capacities are set to nearly triple over the 2022-2027 period, expected to surpass coal's total capacity by 2027 [11]. In 2022, solar PV generation presented the largest growth of all renewable technologies, with crystalline silicon dominating PV technology [12]. Mass investment into developing PV technology, declining levelized cost of energy (LCOE) and the global market to establish PV into buildings and large-scale operations presents a space to optimize and increase PV technology sophistication [13].

To maximise the opportunity in developing sustainable renewable energy infrastructure, accelerations in research are needed to meet the oncoming demand, particularly in PV module technology, for its accessible cost and utility. This thesis aims to explore the creation of thermal energy in PV modules, management techniques and evaluate the effectiveness of novel cooling methods under forced convection conditions.

## 2. Literature review

### 2.1 Genealogy and Limitations

Solar energy refers to the ability to harness photons of light as useful energy in either thermal or electrical form. The novel invention of solar energy generation diversified renewable energy resources and was first commercialized by Bells labs in 1954 for use in the space industry, initially starting out with roughly a 6% conversion efficiency [14]. Due to the high liquidity and access electrical energy offers over thermal energy, this thesis will focus on the electric sphere of solar energy.

The photovoltaic effect that was capitalized upon converts sunlight directly into electricity using solar or photovoltaic (PV) cells. The process uses layers of semiconductor materials, doped with varying chemicals to make them either negatively charged (an n-type semiconductor) or positively charged (a p-type semiconductor), in a cell, where tens of cells are then connected in a circuit to create a single PV module [15]. When the semiconductor material is exposed to solar radiation, the additional energy from photons striking the surface excites the electrons from their atomic structure and forms electron hole pairs. The free electrons flow from the n-type layer through an external circuit back to the p-type semiconductor, generating electricity. Since the inception of solar cells at Bell Labs, silicon has been used extensively in creating 95% of PV modules [16]. It is readily available as the second most abundant element on Earth that is non-toxic and intrinsically has a high energy conversion efficiency [17]. With the high prevalence of silicon models, consideration of alternative materials, such as perovskite and organic cells, will be omitted from the scope of this thesis.

Clear from the outset, the largest implication in discovering solar energy was the constraints in establishing high conversion efficiency. Photovoltaic efficiency is obtained by comparing the electrical power generated against the total light energy introduced to the system (Eq.1). The efficiency of this process is dependent upon factors such as operating temperature, material properties, reflected light, and light wavelengths [16].

$$\eta = \frac{P_{out}}{P_{in}} \quad (1)$$

Despite heavy research gradually increasing the conversion efficiency of PV modules, most recently achieving nearly a 40% conversion efficiency in a laboratory setting, most modern commercial PV modules are limited by lower efficiency conversion capabilities of 17-22%, meaning around 80% of potential energy is lost [18]. The largest inhibitor of maximizing the potential energy of the Sun is the incident formation of thermal energy as a result of its function under constant Sun exposure. Although there are various solar

thermal energy systems which rely on this production of heat energy to function, the same presence of heat energy is highly detrimental to the electric function and lifetime of PV modules [19].

Although, based upon rate of reaction theories, it is expected that with higher operating temperatures, the rate of producing electricity is catalysed with the heightened excitation of electrons, the contrary occurs. Research into the dynamic between electrical efficiency and PV operating temperature discovered an inverse linear trend between cases with and without active cooling when the PV module exceeded designed operating temperatures, shown in Figure 1 below. Without active cooling, the PV module could only achieve a conversion efficiency of 8-9%, whereas the active cooling condition saw an increase in efficiency of 12-14%, achieved through a significant reduction in the operating temperature [20].

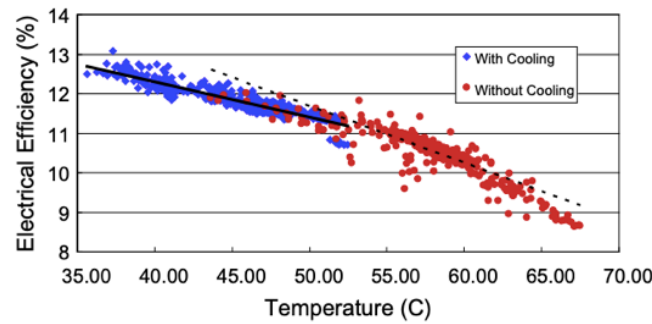


Figure 1 Electrical efficiency as a function of PV temperature [20]

The inverse relationship is caused by the limiting temperature coefficient solar cell materials have; a rate of variation in electrical resistance that develops with temperature changes. When PV module operating conditions of exceed optimal efficiency conversion temperatures, usually approximately 25°C, the excessive heat reduces the band gap distance electrons need to overcome to conduct electricity, shown in Figure 2 [21]. The band gap distance refers to the minimum energy required to excite an electron from an atomic valence state to the conduction band where the electron is free to move and create energy. For most solar cells being silicon, the band gap is usually 1.11 eV at room temperature [22].

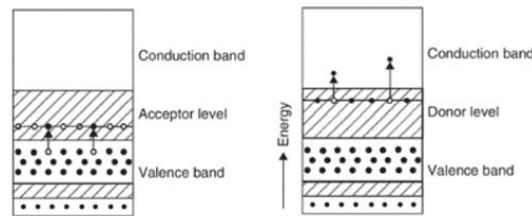


Figure 2 Electricity process through p-type (left) and n-type semiconductors [22]

With heat accumulating and catalysing the formation of electron hole pairs, a reduction in resistance promotes higher recombination mechanisms and reduces the open circuit voltage ( $V_{OC}$ ), compromising the negative temperature dependency required [23]. Recombination mechanisms are when electrons do not

move around the circuit but with the excess energy, reform into the atomic structure and free a photon particle instead, meaning the potential to harvest the energy from the electron hole pairs is lost. The trade-off in efficiency with increasing temperature is known as the Shockley–Queisser limit (1961) where for a range of semiconductor materials, all function at a unique maximum potential under this limit [24], [25], [26], [27].

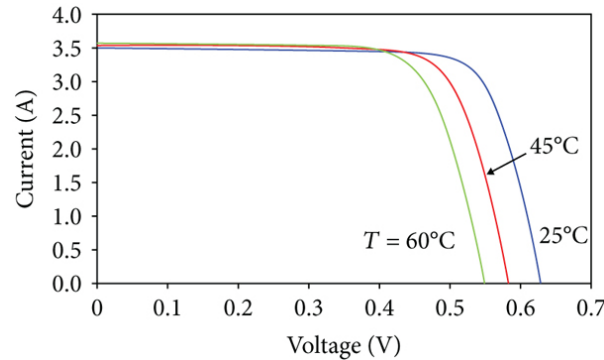


Figure 3 Impact of temperature on current and voltage of a solar cell [23]

Heat energy not only degrades electrical efficiency, but by Arrhenius law acts as a thermo-mechanical stressor on the physical components of photovoltaic systems in the long term [28]. PV modules are constantly exposed to natural climates to maximise power output, however, also experience vast temperature differences throughout the day, at times reaching 85°C [29]. These large cyclical fluctuations and high temperatures leads to cracks and defects developing and propagating throughout the module. The most common failure modes originate from hot spots, delamination, polymer disintegration, water ingress, corrosion of joins and yellowing/browning from UV exposure, with all contributing to a significant reduction in PV module efficacy [30], [31]. To better understand how thermal profiles characterised over the surface of PV modules, testing of PV modules against various inclined orientations under a heat source found that heat concentrated most along the lower section of the module, relatively to the middle or upper section [32]. This heat concentration along the lower portion of the cell was said to have the highest efficiency degradation and was therefore most likely to experience failure.

Appreciating the short term (electrical efficiency) and long term (physical structure deterioration) impacts of thermal energy, reducing PV module operating temperatures as little as 1°C can extend module service life by 2 years [33]. With the abundance of solar energy globally, Figure 4 below, and with climate forecasts predicting a 5.4°C increase across the world by the end of the century, it is imperative for PV technologies to manage operating temperatures so solar energy may develop to dominate a higher share of the energy sector as a steady, reliant source of clean energy for decades to come [34].

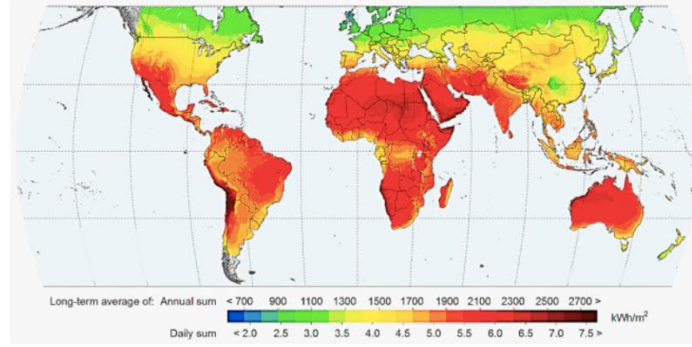


Figure 4 Heat distribution over world [35]

## 2.2 Heat Transfer and PV Modules

As stated previously, photons of energy given off by the Sun are critical for PV modules to generate energy. The potential energy within these photons however needs to be high enough to be able to displace electrons from their atomic structure to generate electricity, generally meaning the infrared spectrum is not as useful as shorter wavelengths with higher energy, such as the visible and ultraviolet light regions. Thus, most PV modules are specifically designed for a light spectrum range of 400-1200nm [36]. However, despite 77% of incident radiation having enough useful energy, further losses are experienced through reflection off the PV surface or more significantly, by being absorbed as thermal energy (43%) [37].

Thermal energy is the sum of latent and sensible form of internal energy that is characterised by virtue of its temperature, and can be transferred to other neighbouring mediums by means of conduction, convection or radiation [38]. An operating PV module has dynamic and fluxing heat transfers; solar irradiance supplies input light energy to the system and through the creation of incident heat energy, is released to the surrounding environment, under the condition ambient temperatures are less than the operating temperatures of the PV module. A simplified version of these interactions is detailed below in Figure 5.

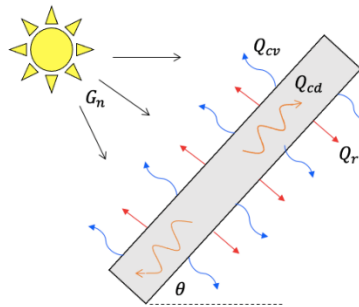


Figure 5 Heat transfer schematic for PV module

As solar radiation reaches the PV module, denoted by  $G_n$ , most of the photonic energy is taken within the PV system either as electrical or thermal energy. The energy moves through the body by means of



conduction, dependent on the PV material thermal conductivity, denoted by  $Q_{cd}$  with orange lines. The heat energy then dissipates off the heated body with energy moving beyond the limits of the PV module's body to the adjacent fluid by convection, denoted by  $Q_{cv}$  with blue lines. This energy transfer to the surrounding environment is either facilitated by natural buoyant forces or external forces, and is driven by the convective heat transfer coefficient (CHTC). Finally, as per non-ideal blackbody radiation, a body will emit radiation based off its temperature and surface emissivity, denoted by  $Q_r$  with red lines [39].

To promote the highest level of heat loss within PV modules, the three modes of heat transfer can be used to coerce heat energy away from the body. The most effective of the three which transports the highest rate and amount of heat energy is convection. It has been found that roughly 66% of total heat loss from PV modules occurs through convection from air passing over both surfaces of the module [40]. For this reason, investigation into cooling methods using convection will be focus of this thesis.

## 2.3 Convective Cooling

Convection is a mode of heat transfer which combines the principles of conduction and fluid motion to transfer energy from a solid to adjacent air or liquid mediums [38]. As with heat principles, heat will move to the medium which has a lower cumulative amount of heat and when bulk movement of fluid motion over a surface occurs simultaneously, the rate of heat dissipation is improved through increases in macroscopic movement of fluid particles and mixing. This bulk motion of fluid can be natural/free, where the fluid motion is characterised by buoyant forces (driven by factors such as the density and gravitational effects), or forced convection, where an external force such a fan, pump, wind or rain influences the motion of the fluid. The main parameters driving convection are the thermophysical fluid properties (viscosity, thermal conductivity, density, specific heat capacity), geometry/shape of the solid surface (surface roughness, length, width), and flow regime (velocity, incline position) [41].

Convective cooling in PV modules occurs as increases in temperature from ambient environmental conditions, or the position of the sun reaches a maximum-heat generating angle, which causes the adjacent fluid layer over the module to absorb this heat through conduction. The heated fluid, now lighter, moves upwards and away by convection currents and is replaced with cooler fluid to repeat heat dissipating process. The fluid's movement of transferring energy away from the module can be represented by temperature and velocity gradients, showing the process of initial interactions to fully mixed ambient conditions, as seen below in Figure 6.



an angle of  $30^\circ$ , an increase in heat transfer from the plate was seen, indicated by a reduction in steady-state temperature. Combined with the lack of sidewalls and narrow plate characteristic, the presence of buoyant forces leading air towards the plate and exiting along the side, rather than flowing along the plate, was predicted to have underpinned this result. At angles of increased severity up to  $90^\circ$ , it was found the heat transfer rate was much lower, caused by weaker components of buoyancy present, lacking a driven systematic flow over the plate.

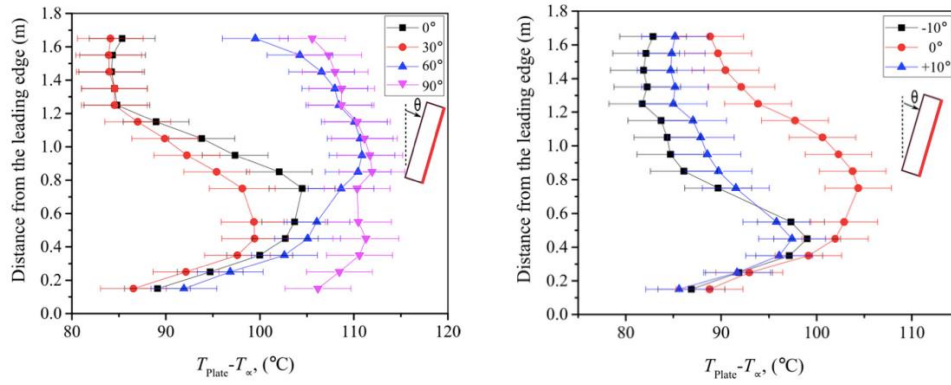


Figure 7 Relative temperatures from leading edge for varying inclines [43]

The last analysis looked at the effect sidewalls had on the heat transfer rate and the incline impact. When  $\theta = -10^\circ$ , the largest overall temperature difference was seen indicating an increase in heat transfer. It was found sidewalls had a notable impact on preventing lateral flows from interacting with the heated surface, increased the boundary layer thickness and delayed the flow change along the panel from transitional to turbulent.

Throughout the testing of varying orientations, the role the CHTC had on results was evaluated. The CHTC,  $h$ , commonly mistaken for being a fluid property, is found experimentally dependent on all variables influencing convection and functioning subgroups under convection. For the vertical plate case with no sidewalls and high flux input, the CHTC gradually decreased with the development of laminar flow until vortices develop transitioning to turbulent flow, where CHTC increased. This is supported similarly for flow over a flat plate (horizontal) by the theoretical variation of the convective heat transfer coefficient following a similar trend. The CHTC was found to be higher in fully developed turbulent flow, with the friction coefficient synonymously increasing being solely dependent on the surface roughness. In conjunction, Kind et al. discovered that a maximum CHTC is achieved when wind direction on a panel was perpendicular to the surface [44].

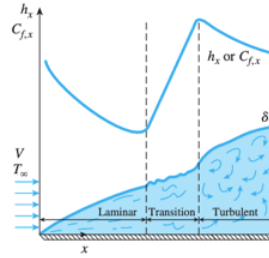


Figure 8 Variation of CHTC with Reynolds number on a flat plate [38]

The way forced convection interacts with systems such as PV modules builds upon the natural convection principles using the same parameters affecting CHTC, in addition to considerations for forced convection such as speed, direction, fluctuations and interference from terrain and structures [45]. Forced convection has been found to transfer heat more effectively than natural convection by augmenting the velocity gradient, and subsequent temperature gradient, with increased flow present directly inflating the Reynolds number and development of turbulent flow [46]. Mazon-Hernandez et al. conducted a quantitative comparison on PV module peak power output under high ambient temperatures, finding that forced convection cooling achieved double an output rate than that of natural convection [47].

## 2.4 Convective Cooling Methods

The types of convection cooling are characterised as either passive or active. Passive cooling uses heat exchanging technology such as heat spreaders or heat sinks to increase the amount of natural convective cooling. The advantages for passive cooling are the low maintenance and financial cost associated with efficiently dissipating heat energy from systems. Active cooling utilises pumps or fans to circulate fluid in a controlled manner to remove heat energy, however, whether the overall power output is offset by the consumption of power required to generate the active cooling mechanism is a paramount economic factor in determining the viability of the method [40].

### 2.4.1 Passive Cooling Methods

#### 2.4.1.1 Thermosyphon

Akbarzadeh and Wadowski's experiment evaluated the convective effects a thermosyphon had on a PV module [48]. A thermosyphon is a passive exchanger system which uses a condenser and evaporator heat exchanger filled with refrigerant (such as R-11) or water to absorb and disperse energy to the environment. As the heat transfer of the condenser was low, the area was extended using fins to increase area exposure to the adjacent air. In a 4-hour period, the thermosyphon produced a module surface temperature of 46°C, proving a significant improvement from the control case presenting a surface temperature of 84°C. However, due to the small-scale testing there were limitations in the sun exposure rates and hence produced lower overall power output. Due the complexity and cost of the system, it was reflected on being

commercial constrained for production. Agarwal and Garg independently found the thermal efficiency of a thermosyphon also depended on the packing factor of the PV cells [49].

#### 2.4.1.2 Fins

An alternative passive cooling study, conducted by A.M. Elbreki et al. researched both theoretically and experimentally the effect fin shape and density in heat sinks had on PV modules heat transfer [50]. Against a reference bare PV module at an ambient temperature of 33°C, average solar irradiance of 1000 W/m<sup>2</sup>, and an optimised tilt angle of 14°, the use of longitudinal and lapping fins presented drops in PV module temperatures of 23.8% and 35.3% respectively. In studying the heat transfer effects of both fin types, it was concluded the lapping fins had a more superior performance, with an operating temperature 24.6°C lower than the reference case. A life cycle cost analysis found the payback period for a PV module with lapping, longitudinal and bare configurations were 4.2, 5 and 8.4 years respectively.

#### 2.4.1.3 Water

Trapani and Redon Santafé investigated a symbiotic relationship between an unoccupied water reservoir surface and floating PV modules [51]. The presence of floating PV devices simultaneously reduces the amount of water evaporation off bodies of water and development of algae growth by blocking light penetration into water, whilst acting as a natural cooling source for the PV modules. The increases in annual energy yields ranged from 20-70% with different exposure configurations.

Similarly, Rosa-Clot M et al. sought to understand how submerging PV modules into bodies of water could be used to reduce thermal drift and reduce light reflection at depths of 4cm and 40cm [52]. The reference plate experienced operating temperatures of 70-80°C, compared against the 4cm submerged panel operating temperature of 30°C. The average efficiency gain for the 4cm submerged plate was found to be roughly 11%, whereas the submerged plate at 40cm experienced a reduction in efficiency of 23%. A reduced efficiency of 10% was found for both depths from water absorbing solar radiation from the panel.

### 2.4.2 *Active Cooling Methods*

#### 2.4.2.1 Water

Studies conducted by Krauter, Odeh et al. and recently Krzysztof Sornek et al. tested the advantages of using an active cooling system to pump water over the PV surface to maximise the highest convective heat loss, whilst simultaneously providing antireflective and dust/debris cleaning benefits [53], [54], [55]. Dependent on the choice of pump, it was found a net electrical gain of 8% could be achieved, however the

required water consumption and evaporation rate ( $1 \text{ L/hm}^2$ ) needs to be properly addressed. For a high volume of solar panels such as farming formation, using liquid based cooling methods have drawbacks with water-based damages from corrosion, water ingress and maintenance issues, proving difficult to guarantee a 20-year warranty.

#### 2.4.2.2 Air

Salaudeen found air to be the most suitable choice of working fluid for cooling due to its vast availability and durability [56]. Active cooling systems using air channels circulating various flow paths and fins have been innovatively designed to further optimised heat transfers from the back of PV modules. Girish JR investigated the importance in ensuring an air gap beneath PV modules was sufficiently large enough to ensure environmental convective cooling could take place and ensure operating temperatures were not exacerbated by limited air flow [57]. It was found a roof to PV panel height of 100-110mm was optimal and increases beyond this point have a negligible benefit.

Research conducted by A.R. Amelia et al. looked into the relationship between increasing the number of fans supplying forced convection to PV modules to determine if a saturation in the number of fans would develop, from temperature build-up from each fan negating improvements, or if efficiency would continue to improve indefinitely [58]. The study increased the number of fans from 1 through to 4, used a reference PV module and recorded ambient temperatures to clearly see the fan heat generation and cooling impact. It was found that although increases in power output for 2, 3, and 4 fans saw gains of 37.17%, 41.28% and 44.34 % respectively, more electrical power was needed to be consumed, and the capital cost increased to meet this objective. It was evaluated that the increased air circulation achieved should be applied to remove heat as needed, and the optimal number of fans for a PV module was 2 based on capital costs and overall gains.

#### 2.4.2.3 Fins and Heat Sinks

Tripanagnostopoulos compared the effects between placing a thin metal sheet (TMS) in the center of the channel against fins on the back wall of the channel to understand how mixing can be distorted to influence back wall temperature and output air temperature, shown in Figure 9 [59]. The fin system was found to have the highest yield efficiency of 30%, producing higher output air temperature from the system, but found to transfer a higher amount to the back wall through conduction. The TMS yielded an efficiency of 28% and promoted a  $5^\circ\text{C}$  temperature difference from the reference case for the back wall temperature by due to a shading effect from the sheet occurring. This design is ideal for Building Integrated Photovoltaic (BIPV) designs where large airflow spacings between PV modules and building structures cannot be

afforded and have conscientious designs which impede heat from being drawn into buildings, ensuring building energy consumption is kept to a minimum.

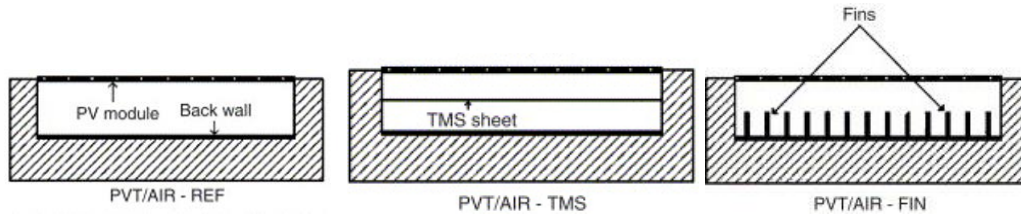


Figure 9 Various airflow channel configurations [59]

Sopian et al. and Hegazy researched into the glass covers and flow configuration past PVT modules to determine highest heat collector transfers. Sopian looked into the variables which impacted thermal solar collector performance being the absorber plate temper, mass flow rate, duct depth, collector length, inlet temperature, solar radiation and packing factor [26]. It was found that as the absorber plate length increased, the PV efficiency decreased due to the average temperature of the absorber plate increasing. If the absorber plate length was kept constant and mass flow rate into the channel increased, the PV cell efficiency also increased. Overall, at a mass flow rate of 200-300 kg/h and PV module length of 1m, the increases in thermal, PV and combined for the single pass system were 24-28, 6-7, and 30-35%, compared to the double pass systems increases of 32-34, 8-9, and 40-45%, showing superior performance. Hegazy continued the channel flow study further to find that for a high mass flow rate, a double single pass orientation presented the highest overall performance over a double pass configuration, attributed to a higher mass flow rate [60]. The two channel type configurations from Sopian were reproduced, as well as a double single pass flow and air flowing over the PV module were used to create the 4 models of the study. All collector models tested found a critical mass flow rate existed where thermal collector overall performance decreased past this point. An optimal ratio for the flow channel ratio, depth to length, was determined to effectively maximised thermos-electric gains at  $2.5 \times 10^{-3}$ .

#### 2.4.3 Vortex generators

Vortex inducing devices have been used extensively to manipulate fluid dynamics to delay flow separation in adverse pressure gradients that develop after a body passes through fluids at speed. Flow separation off a body occurs when a body has a geometry which the fluid passing over cannot follow the shape of the surface and “detaches”, causing eddies to develop and a suction force (from a low pressure space forming) pulling the body from behind. This slows the overall velocity of a moving body from the formation of drag force. Vortex generators (VGs) work by their characteristic shapes and oblique positioning to create swirling wakes, enabling them to pull excess energy from an adjacent free stream into a boundary layer, to increase the overall energy within said layer, and reduce cumulative adverse pressure gradients [61]. As fluid along a curved surface of a body moves much slower than free-stream velocities, using VGs to

introduce energy into the boundary layer causes enhanced mixing of fluids, causing turbulent flow to develop sooner with a higher intensity, and are generally used to delay the separation of flow off the body. Vortex generators have been used in novel ways to enhance heat transfer by optimising angles of incline against flow direction (“attack angle”), geometries and positioned locations for promoting cooling [62] [63] [64] [65].

#### 2.4.3.1 Shapes and vortices

Longitudinal VGs are more efficient in enhancing heat transfer over transverse VGs and will be the focus for optimising enhanced heat transfer techniques [63]. Most research on VGs have focused on winglet and wing designs being easily mountable or punched into channel walls or fins to effectively generate longitudinal vortices [66]. Longitudinal vortices have rotating axes parallel to the oncoming free-stream flow, where the flow is three-dimensional. It is known however minor transverse vortices are produced based on adaptations to the attack angle.

Delta wings and winglets, rectangular wings and winglets were all compared and it was concluded delta and rectangular winglets had comparable heat transfer enhancing effects, with winglets proving to be more effective than wings under laminar flow conditions by producing a lower pressure drop [67]. Arguments have been made however that per unit area, delta wings have the highest heat transfer enhancement rate [68]. Tiggelbeck et al. found for delta winglet VGs that as the Reynold number increased, the heat transfer rate also increased nearly linearly, where at a Re of 6000, a heat transfer enhancement of 80% could be seen [64]. Zhou and Ye proposed the use of trapezoidal winglets and curved trapezoidal winglet VGs to view the enhancing heat transfer factor compared against existing VG models; delta and rectangular [66]. It was concluded delta winglet pairs were the optimal choice for laminar and transitional flow regions, however for turbulent flow, the curved trapezoidal winglets produced the best thermohydraulic performance, due to a low pressure drop and streamline configuration. Moreover, water-based experimentation studying the size of VGs and the relative vortices that develop saw that smaller VGs produced smaller vortices that dissipated quickly in the flow, having the highest heat transferring effect locally around the VG. The wings/winglets discussed above can be seen below in Figure 10 as rectangular, trapezoidal, delta and curved trapezoidal.

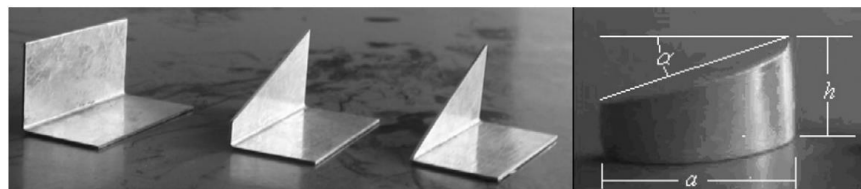


Figure 10 Vortex generator shapes [66]



### 2.4.3.2 Orientation and positioning

Altering the orientation and row configurations of VGs can distinctly impact the heat transfer and the flow structure downstream. Biswas et al. researched into how longitudinal vortices could be optimised in a channel flow numerically and experimentally using delta winglet type VGs [69]. It was concluded the Nusselt number increased by increasing attack angle, and the resulting vortices were stronger producing better heat transfer. The VG inclined at an angle of  $15^\circ$  produced a spanwise average Nusselt increase of 32% compared to an attack angle of  $37.5^\circ$  which achieved a 65% improvement. The trade-off of using higher attack angles however increased the effect of pressure drop developing and reduced the quality factor, concluding the attack angle of  $15^\circ$  gave the best results relatively. Conversely for rectangular wing VGs, it has been found an optimal attack angle of  $25^\circ$  produces a maximised thermal enhancement factor, beyond this decreasing, shown in Figure 11 [70]. This orientation is said to produce widened and more energetic vortices, with a high helicity that sustains for longer along the channel.

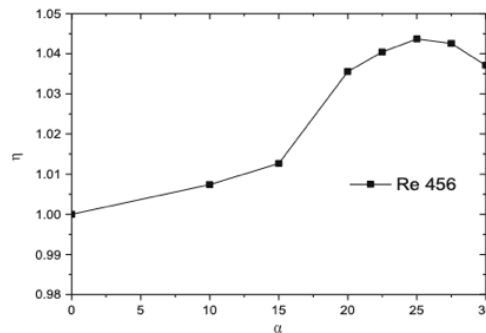


Figure 11 Attack angle against efficiency [70]

The height of the VG compared to the wind tunnel also found that optimised Reynolds numbers were not consistent with varying VGs heights and number of rows. When only one row of VGs was used, a lower dependence on the Reynolds number could be seen than the use of multiple rows. An optimised heat enhancement rate was in a transitional flow regime, commonly between a Reynolds number of 950 and 1700. It was found increases in enhancing heat transfer decreased with subsequent rows past the 2nd, and in turbulent flow, the additional enhancing effect was limited to 5%, showing in Figure 12. A maximum peak heat transfer enhancement of 40% was found at the second row of VGs, finding taller VGs had greater enhancing effects [71].

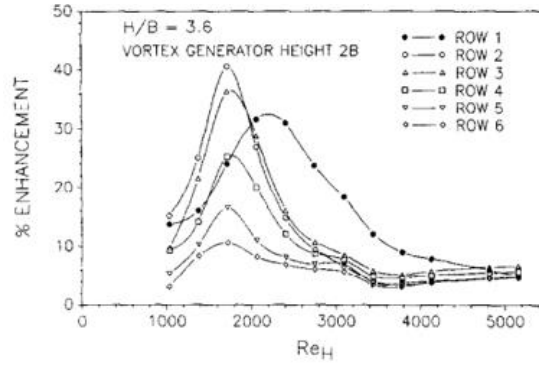


Figure 12 Reynolds number against heat transfer enhancement and rows of VGs [70]

Bittagopal Mondal et al. similarly assessed the positioning and density of VGs in cooling channels for a lithium-ion battery thermal management system (BTMS) using a numerical simulation, with batteries facing the same performance deterioration with higher temperatures present [72]. The model was conducted under a laminar flow range of  $65 \leq Re \leq 1650$ , and used minute winglets pairs orthogonal to one another, sized to 1.2mm(L)x0.3mm(W)x0.05mm(t). The formations assessed were FC-I, FC-II, where the winglets were installed on the backside of the channel, filling the width of the channel as double pairs or singularly in the middle of the channel respectively, and FC-III and FC-IV where the winglets were placed on both the front and back side of the channel, again on the left and right side of the channel or placed in the middle. The conclusions drawn from the analysis found the FC-I and FC-III cases outperformed FC-II and FC-IV in promoting cooling due to more VGs present, helping to disrupt the thermal boundary layer and enhance the heat transfer rate through stronger vortices creation, and minimised spacing. The enhanced mixing resulted in lower battery module temperatures and higher fluid temperatures within the channel, reflecting the heat transfer process occurring, shown below in Figure 13.

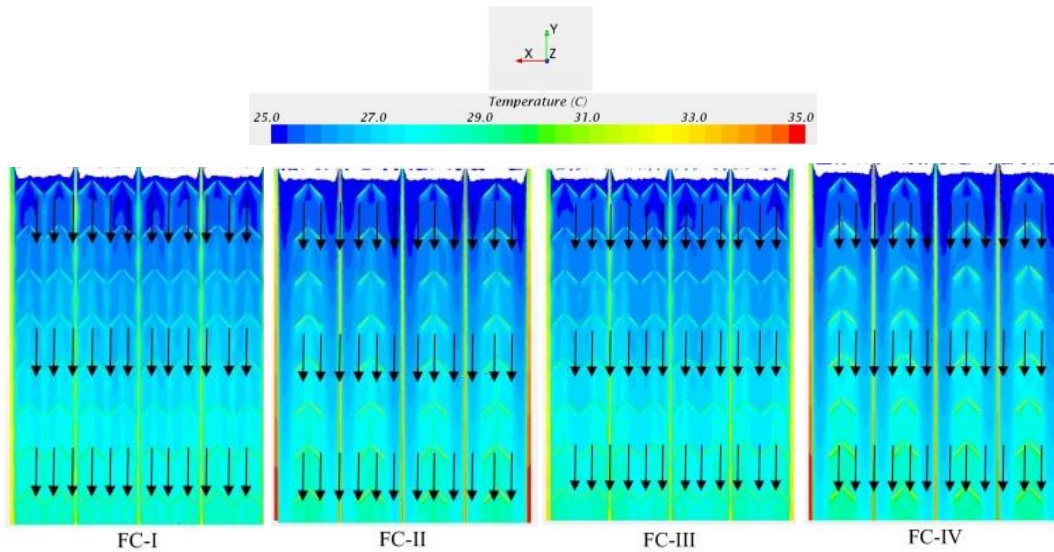


Figure 13 Temperature profiles at the middle plane of the cooling channel [72]

## 2.5 Experimental Measurement Techniques

Experimental testing involves using simulation and laboratory technologies to analyse how altering variables under the force convection state impact the heat transfer rate and flow fields. The experimental techniques which have been researched into include CFD modelling and infrared thermography.

### 2.5.1 Computational Fluid Dynamics

Computational Fluid Dynamics (CDF) is a modelling software that creates simulations of complex real-world interactions by digitally constraining a system using governing fluid motion equations, algorithms and numerical methods to create quantitative predictions and solutions. CFD is a flexible and highly cost-effective technique, regarding both time and resources, that can complete an innumerable amount of alternate design combinations. For flow separation and boundary layer simulations, CFD modelling on PV modules, validated by Arpino et al., utilises Reynolds Averaged Navier Stokes (RANS) approach combined with k-epsilon ( $k-\epsilon$ ) and k-omega ( $k-\omega$ ) turbulence models where  $k$  represents turbulent kinetic energy, and  $\epsilon/\omega$  refer to the turbulent dissipation rates [29]. For all the benefits numerical modelling offers and user efforts to constrain the digital model to accurately form realistic experiments, it is noted numerical model of PV experimentation usually predicts higher temperature values within PV cells than physical experimental model [19]. This 1-2% discrepancy is thought to occur from module connection affecting electrical efficiency or debris accumulation over PV surface reducing the overall irradiance in physical experiments [29]. Despite this, the trends between theoretical and physical experimental results show similar linearity, per Figure 14, and thus demonstrates how the technique is advantageous to perform initial simulations [20].

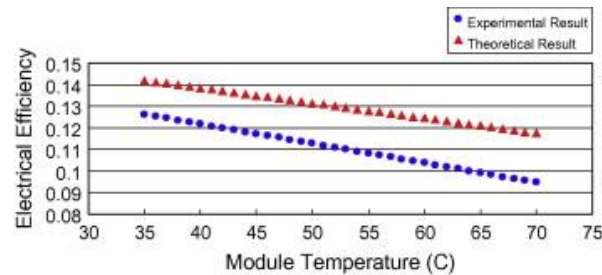


Figure 14 A comparison between theoretical and experimental results. [20]

### 2.5.2 Infrared Thermography

To measure the heat distribution over a PV module surface and compare the subsequent changes in temperature, infrared thermography can be used. Infrared thermography is a contactless and non-destructive measuring technique which evaluates temperature by detecting emitted infrared radiation given off by bodies, following Planck's law. As radiation is a function of surface temperature, the wavelengths that reach

the lens of the thermographic camera can be calibrated to accurately determine the associated temperature of the body's surface, accounting for ambient conditions such as humidity, temperature, distance [65]. The total radiation power ( $W_{tot}$ ) that reaches the camera is comprised of the radiation from the body ( $W_{body}$ ), reflected radiation from surrounding sources ( $W_{ambient}$ ) and distortion from atmospheric radiation ( $W_{atmospheric}$ ). The following equation details how the radiation solely from the body is found, where  $\varepsilon$  is the emissivity and  $\tau$  represents the transmission.

$$W_{body} = \frac{1}{\varepsilon\tau} W_{tot} - \frac{(1 - \varepsilon)}{\varepsilon} W_{ambient} - \frac{(1 - \tau)}{\varepsilon\tau} W_{atmospheric}$$

A large benefit of using infrared thermography on PV modules over other thermal measuring devices is the fast data acquisition and visualisation of thermal distributions and concentrations, which has led to it being used extensively to detect faults in PV cells post-installation [66].

### 2.3.3 Thermocouple sensors

Thermocouples measure temperature by using two unlike conductors (metals, alloys or semiconductors) that when an electric current develops in the junction of the closed circuit, the electrical energy can be used as a means to measure temperature. Thermocouples are regarded as versatile being able to be used at both extremely high and low temperatures, with high accuracy and fast response time to temperature changes. The compact, simple construction and application of thermocouples makes them durable and cost-effective over other temperature sensors, however, are said to not be as stable as resistance temperature detectors (RTD) and have non-linearity issues [67]. As thermocouples need to be placed in contact with a surface to measure temperature, Nicholas et al. found the results produce an error between 5% and 10%, however this is argued to be much less with a  $\pm 2.2^\circ\text{C}$  or  $\pm 0.75\%$  error [68] [69]. There are many types of thermocouples for various applications, but most PV experiments used K-type or T-types, respectively used for high prevalence and usefulness, or for lower temperature recordings [26] [29] [70] [71] [42] [19].

### 3 Methodology

#### 3.1 Motivations and Aims

With forecasting trends predicting a surge in the uptake of PV technologies, and concerns arising from PV module waste, there are now imminent demands for renewable energy technologies to improve in longevity and performance. Chapter 2 critiqued current technologies employed to promote cooling in PV modules, using both active and passive techniques; however, current literature lacks information on the extent to which the presence of VGs integrated into PV module systems has on the efficiency and overall performance of photovoltaic systems. Many forced convection cooling methods focused on water integrated designs for recovering the highest efficiency gains, though operating PV modules in close proximity to water presents issues arising from water damages and economic feasibility in sourcing and wasting high volumes of water to make this realisable [76]. Research into studying the CHTC effect on both sides of PV module, with the module inclined, has not been extensively covered and presents an opportunity to be developed upon further. Enhancing heat transfer on the underside of PV modules has been accomplished through the utilization of heatsink and fin technologies attached to the PV modules. However, challenges arise when the absorbed heat infiltrates the structure of these devices, posing complications for PV applications, particularly in the context of Building-Integrated Photovoltaics (BIPV). Current literature on VGs promoting cooling in PV is limited to natural convection cases when the “worst case” operating temperature is experienced but does not expand to include a realistic environment in which all PV modules will operate in, undergoing forced convection of some type, through naturally occurring rain or wind.

Vortex generators have been chosen as the primary cooling device to complement the benefits solar energy affords. Solar energy is relatively cheap and globally available, making it obvious to use a convective medium which is equally as abundant; air. The passive and simple design of a VG ensures there are no restrictions in its availability to global demographics, furthering solar technology’ accessibility, whilst exerting aerodynamic control onto surrounding airstreams. The inclusion of VGs in PV systems presents a promising solution to managing operating temperature and will be designed in a manner which does not infringe upon current PV module Warranty conditions.

In completing experimentation and analyses by varying parameters and processing results, this thesis seeks to form a framework to streamline results which will then form a foundation for future results to be developed upon. Experimentation that has been previously completed at UNSW has resulted in work completed from prior students and research colleagues to be passed on to use in this research thesis. To

accurately simulate the function of a PV module under real world conditions, the primary aims of the thesis are to:

- I – Characterize the wind tunnel.
- II – Complete initial findings into the efficacy of rectangular VGs on PV modules under varying force convection speeds.
- III – Design ways to improve the functionality of the PV module frame to suit installing VGs.

### **3.2 Overview of Experimentation**

The way in which the aims will be achieved are through the following:

I – The large wind tunnel (LWT) is characterised by operating extensively to predict the minimum time required for the entire system (power supply and hydraulic pump) to stabilise. The cascading relativity effect of environmental outdoor temperature on the laboratory ambient temperature, in turn affecting the LWT temperature, is assessed and forms the basis of obtaining results upon. Control cases are then established - the PV module and acrylic board with no VGs present - to find the baseline effect the LWT has on cooling the PV module initially. With steady-state conditions required to obtain data, stabilisation of the wind tunnel and the DC power unit were observed to determine the stabilisation time for the system. The stabilisation of the LWT is expected to occur when the operating temperature of the hydraulic pump in the LWT reaches steady state.

II – Data is collated for rectangular VG cases adjusting variables such as VG height and direction across forced convection speeds of  $V$  at 1m/s, 2m/s and 3 m/s. By processing and comparing the results using MATLAB, a final assessment will evaluate the effectiveness VGs have promoting cooling on the PV module, and will determine which formation produces the optimal result. It is anticipated that the full VG case will offer enhanced cooling potential compared to the half VG case. The side of the VG where the vortices will develop (dependent upon VG orientation and wind direction) to promote cooling remains ambivalent.

III – The design of the PV module frame has been suited for testing natural convection PV experiments. Preliminary design work will be undertaken to enhance its suitability for forced convection testing. The planned design modifications aim to reduce the time and expenses associated with installing VG arrays and modularize the positioning of the VGs across the “roof’s” surface.

### 3.3 Experimental Equipment

To complete the set of aims detailed above, the relevant equipment and equipment characteristics are required to achieve this. This is detailed below.

PV Module – WINAICO Perc Series P6 WST-285P6 PV Module was used with property details listed in Table 1 below [77].

*Table 1 Properties of PV module*

Properties	Details
Material	Polycrystalline silicon
Frame material	Black anodised aluminium
Dimensions	1665mm length, 999mm width, 35 mm depth
Cells	Total 60; 10 cells long, 6 cells wide
Rated power	Total 285W; 4.75W per cell
Open circuit voltage/current	38.9 V / 9.57 A
Maximum series fuse	25A
Efficiency rating	17.13 % under STP; solar irradiation 1,000 W/m <sup>2</sup> , light spectrum AM 1.5, operating temperature 25°C
Electricity output decline	Year 1: 3.0 %, Years 2-25: 0.7%
Temperature coefficient of $P_{max}$	-0.43 %/°C
Temperature coefficient of $V_{oc}$	-0.33 %/°C

Aluminium Frame – supported both the PV module and the acrylic layer and was placed inside the LWT for testing. The frame was made from 3.5cm thick MayTec square beams. The frame was inclined ( $\theta$ ) at 45° for both acrylic board and PV module, and formed a channel between the acrylic board and PV module with a clearance of 10cm.

Acrylic Sheet – Three flat acrylic sheets were used to imitate the roof, where the VGs were mounted upon, and was held by the aluminium frame. The sheet was transparent to confirm the VGs were installed correctly, and for potential PIV experimentation so VG flows could be viewed easily. Like a roof, the board allowed no air to pass through the material. The thermal conductivity of the sheet was low, and had dimensions 1825 mm long, 1000mm wide and 6mm thick.

Vortex Generators – have been created previously in natural convection testing and were used and installed onto the acrylic sheet. The VGs were 3D printed using PLA material into a rectangular wing design, resulting in a low thermal conductivity and were rectangular in shape with a thickness of 1.5mm. The VGs had an incline of 45° and were 14cm long for the full height, 6cm for the half height, and were 4 cm wide. The installation of the VGs to the acrylic sheet was added using double sided sticky tape, placed on strips of wood, and stuck to the acrylic board.

DC 1.2 kW Power Supply (QPX1200SP) and Junction Box – heat was added to the PV module using a DC 1.2 kW Power Supply, junction box and connecting wire to simulate the heating a PV module which would develop from sun irradiation. The voltage was set to 30V (less than the maximum open circuit voltage of the panel) to initially test the connections and ensure current was flowing from the junction box throughout the panel. This was increased to deliver 50V at 20A. The error in the voltage and current delivered is 0.1% and 0.3%, and the voltage decreases to approximately 45V, delivering roughly 450W to the module, as the Power Supply reaches steady state. The junction box was located on the underside at the top of the PV module and the Power Supply was placed outside the LWT.

Large Wind Tunnel (LWT) – used a hydraulic and charge pumping system to create a subsonic closed return-circuit wind tunnel. The two of these worked in unison to create a circulating wind tunnel chamber that could artificially produce wind, meaning the flow conditions could be controlled. As the wind tunnel operated in a closed return loop, the LWT had to stabilise for the operating temperatures to reach steady state. The section of the LWT which will contain the PV module configuration will be in the Large Test Section (LTS), shown below in Figure 18. The true velocity of the tunnel was validated using a velocity meter inside the LTS, in line with the start of the frame. The flow velocities used for testing were 1m/s, 2m/s and 3m/s, with a low freestream turbulence intensity of approximately 0.1%. The stabilisation time between each speed was found later. A scaled CAD model of the LWT can be found in Appendix B.

Velocimeter – corroborates the true velocity of the flow being cycled through the LWT and subsequently, over the PV module and frame, shown below in Figure 15.



*Figure 15 Velocimeter*

FLIR E95 Thermal Imaging Camera Devices – measured the heat distribution across the PV module and evaluated the heat dissipating effect of VG formations. The FLIR camera recorded and captured real time imaging of the surface temperature, transforming the physical temperature of the PV module into an infrared image. The camera was mounted onto a tripod and angled to record the PV surface orthogonally, at a clearance distance of ~ 2m to capture the entirety of the surface within the scope of the lens. With the camera calibrated, thermal images were taken remotely using the affiliated FLIR software. The calibration parameters (emissivity of PV surface, temperature range, ambient temperature) were kept consistent



throughout experimental data collection and stored with each photo taken. The camera had a resolution of 348x464 and captured 161,472 temperature pixels per image. It had a thermal sensitivity of 0.03°C and measured temperatures from -20 to +1500°C, however, was set to a thermal range of 15-35°C.

FLIR Software –imported the pixelated PV module image from the camera and generated datasets of the thermal profile for data analysis. The software was used alongside the thermocouple measurements from CoolTerm to accurately scale the ambient temperature to a live reading, and adjusted the pixel temperatures for every photo to scale against the ambient temperature. This raw data was then exported as a CSV file with the associating parameters attached to be processed further in MATLAB.

Thermocouples, Resistance-to-Digital Converter MAX31865, CoolTerm – 6 thermocouples were placed on and around the PV module to record the surface temperatures and ambient freestream temperatures. K-type thermocouples were attached using masking tape and had extending wires leading to a resistance-to-digital (RTDs) converter to record the temperature data sets, timestamped accordingly, using the CoolTerm software. The thermocouples measured the ambient lab temperature ( $T_{ambient}$ ), module temperature ( $T_{module}$ ), temperature on the upper and lower side of the roof ( $T_{roof,top}/T_{roof,bottom}$ ), and the temperatures of inlet and outlet air of the gap channel ( $T_{entrance}/T_{exit}$ ), shown in Figure 16. The use of both contact and non-invasive temperature recording methods offered diversity and ensured contact errors are minimized using IR thermography.

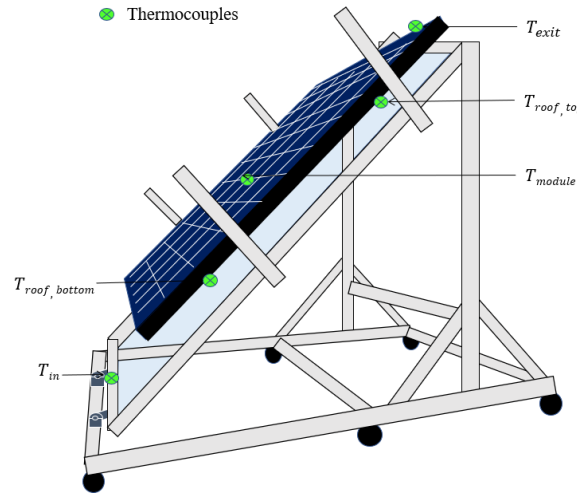


Figure 16 Thermocouple placements across PV module configuration

MATLAB – was used as the main software to process the results by de-warping the images, zoning the main region of interest and completing data analysis between baseline and VG formations. MATLAB is a powerful tool for algorithm and visualisation, making it well suited to handling and manipulating the large datasets generated from the FLIR imaging.

### 3.4 Experimentation

#### 3.4.1 PV Module Configuration

The equipment discussed above was assembled as shown in Figure 17, for experimental testing in the UNSW Aerodynamic Laboratory. The PV module and roof inclines were set to  $\theta = 45^\circ$ , closely resembling required IEC testing conditions [73] and was identical to the preceding natural convection setup.

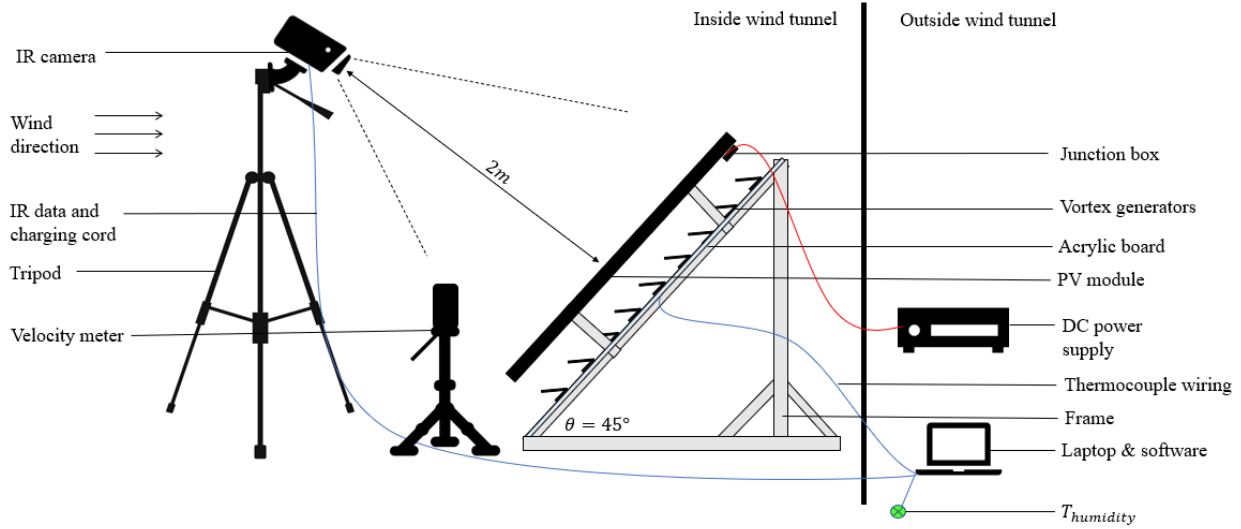


Figure 17 Experimental set up using IR camera

The testing was completed in the LTS of the LWT (an octagonal cross section of  $3m \times 3m$ ) with the PV module frame situated in the center, shown below in Figure 18. For consistency, the frame orientation shown, with respect to the oncoming wind direction, was used across all configurations.

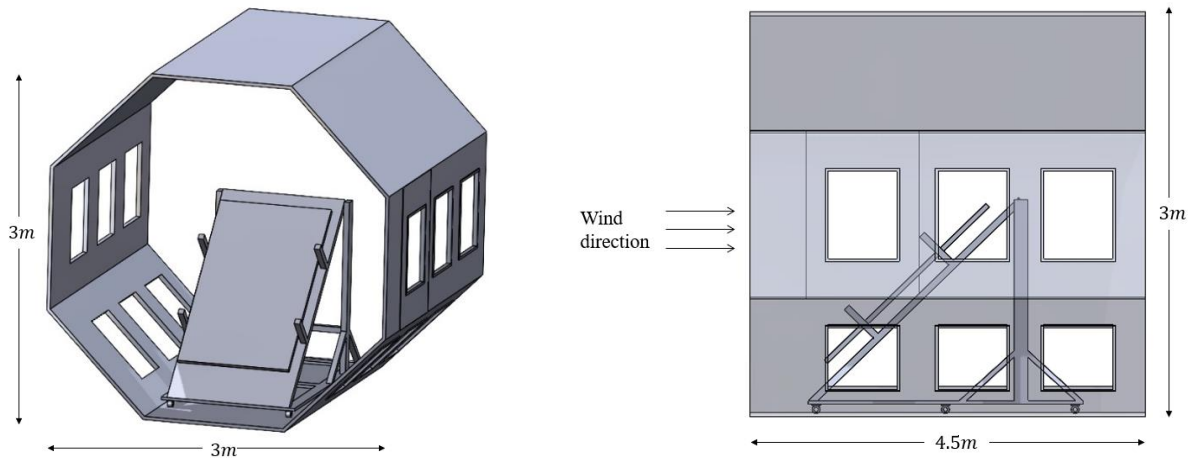


Figure 18 LTS with PV frame inside (isometric view, left) (side view, right)

To bypass the IEC testing requirement, the VGs were installed on the acrylic board using double-sided tape ( $\sim 150 \mu\text{m}$  thick) to wooden strips and then stuck to the “roof” at equidistant spacings of 100mm for both  $P_x$  and  $P_y$  axes, shown in Figure 20. Each strip had at least 10 VGs (11 were usually used), and 6 of these strips were distributed spanwise. The VGs have no physical contact with the PV module, as seen in Figure blah below. The height  $H$  (full – 9.9cm and half– 4.24cm) is derived from the length  $L$  (full – 14cm and half– 6cm), and the angle of the VG is a constant  $45^\circ$ . The VGs were installed perpendicular to the freestream direction, (the attack angle was zero ( $\beta = 0$ )), so that the VGs could form the largest vortices and have the highest contact area with the oncoming freestream.  $G$  represents the gap between the acrylic board and the PV module, which was set to 15cm. Hence, the  $H/G$  ratio refers to the vertical fill ratio of the channel, namely the amount of vertical space the VGs occupy in the gap. Conversely, the horizontal fill ratio is dictated by  $W/P_x$  and conveys how densely packed the channel is in the horizontal (spanwise) direction.

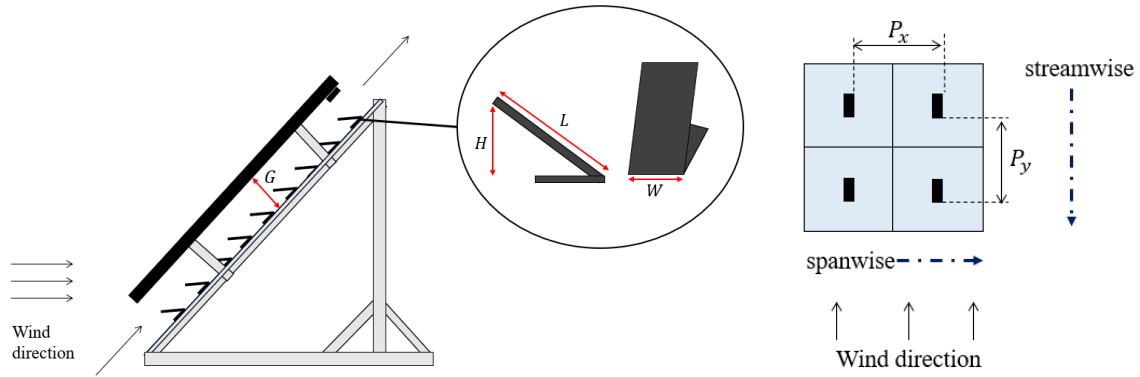


Figure 19 Wind direction and spacing dimensions

The formations that were assessed were fwd\_full (Figure 20), fwd\_half (Figure 21), back\_full (Figure 22), back\_half (Figure 23) and fwdback\_full (Figure 24).

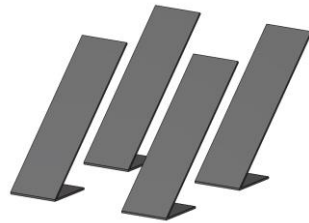


Figure 20 fwd\_half formation

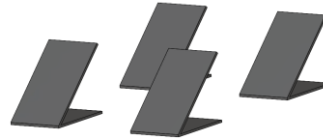


Figure 21 fwd\_full formation

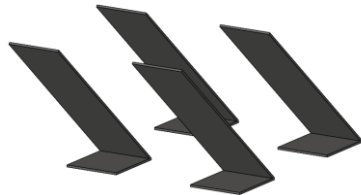


Figure 22 back\_half formation

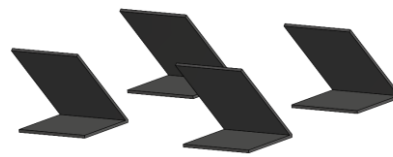


Figure 23 back\_full formation

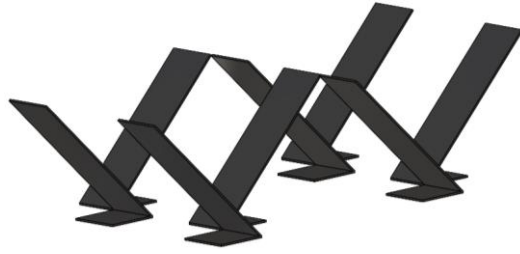


Figure 24 fwdback\_full formation

Based upon Literature indicating PV modules are generally assembled as arrays, side-to-side and with no air gaps, the use of side panels was implemented into the results obtained. This was done to imitate the environment a PV module exists in, where lateral airflow escaping past the edges would occur only on panels at the edges of these arrays. The boundary layers that are expected to develop, supported by literature, are depicted below in Figure 25 and 26, where left portrays the boundary layers generated from the side panels, and right portrays the PV module and acrylic surface boundary layers. It is also known that naturally occurring forced convection is chaotic and random and would not realistically move across a PV system in solely one direction, however in keeping variables controlled to draw direct comparisons, this unidirectional flow condition was implemented.

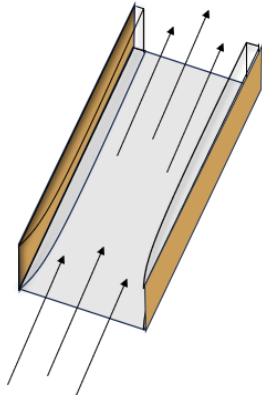


Figure 25 Top view of side panel boundary layers

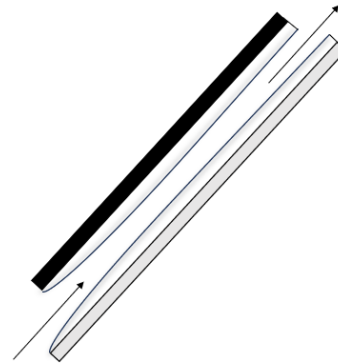


Figure 26 Side view of PV module and acrylic base boundary layers

### 3.4.2 Data Acquisition

For each formation tested, the Power Supply and LWT were turned on and given time to reach steady state at the first wind speed of 1m/s, with the wind speed validated by the velocimeter. Upon initiation, the CoolTerm software recorded the 6 thermocouple readings every six seconds, timestamping the moment each recording was taken. To simulate irradiation and the subsequent incurred heating of the PV module, the DC Power Supply delivered 20A of current to the PV module through the junction box located at the top, simulating approximately  $900 \text{ W/m}^2$ . Once the temperature of the system and the voltage of the power supply were consistent, three IR images were taken iteratively 10-15minutes apart, to generate thermal

profiles of the module. The air speed was adjusted for the remaining velocities (2m/s and 3m/s), given time for stabilise again, and the data collecting process was repeated for each. For the wind velocities, the anticipated Reynolds number that the PV module configuration experienced ranged from  $11643 \leq Re \leq 34928$  (Appendix C), creating a flow regime that is turbulent before assessing VG impact. All measurements conducted were taken within a 12-month period, where the ambient laboratory conditions fluxed from between 20 °C to 33.2 °C, while the relative humidity remained around 50-60%. A systematic and consistent file naming convention was formed and applied to every measurement for clarity in identifying each file and maximizing efficiency in sorting and selecting later in data analysis.

For Baselines: forced\_convection\_baseline\_runX

For VGs: Orientation\_Height\_runX

i.e fwd\_full\_run1

### 3.4.3 Environmental Conditions and Assumptions

To control all other variables within the experiment, or monitor fluctuations for later reference, the adjacent environment was monitored throughout the year to be able to draw comparisons between the VG cases and baselines. This involved closely following the ambient temperature, humidity and integrity of results by assuming or doing the following:

**Distance and angle** of IR images were attempted to be kept consistent across testing with the camera situated 2m away from the frame and inclined to center the PV frame within the lens frame.

**Uniform emissivity** across PV module surface – emissivity being a measurement of how efficiently an object emits thermal radiation. IR imaging requires constant emissivity across the surface for accurate measurements.

**Steady state** – stable state of cascading relativities, situates that there was consistent heat transfer (corroborated with iterations at the same speed). Room was volumetrically large enough (400m<sup>2</sup> with a 10m ceiling) that spiking or sharp changes in ambient temperatures does not occur.

**Homogenous fluid flow** across the PV module set up – the wind circulating was assumed to be constant and uniform across the wind tunnel, assuming that the PV module has consistent heat transfer effect occurring spatially. The wooden strips and tape are presumed to not interfere with the aerodynamics or heat transfer effect, and are hence excluded when modelled in CFD.

## 3.5 Data Processing

### 3.5.1 FLIR Processing

The post processing of the raw thermal imaging results began by importing the images taken in FLIR Tools using the phone application into the laptop software, to scale the ambient temperature to accurately reflect the operating environment of the PV module. Arbitrarily, the ambient temperature was set to 25°C by the

FLIR software, however, to account for the relativity effect of the temperature inside the LWT, was altered for every measurement by referring to the thermocouple readings obtained using CoolTerm. By aligning the time that each image was taken, the exact thermocouple measurement for the ambient at this time could then be applied to the image within the FLIR software, scaling the temperature readings of the entire module with respect to this value. As stated previously, the parameters and temperatures of every pixel in all images were exported from FLIR as CSV files for further processing in MATLAB.

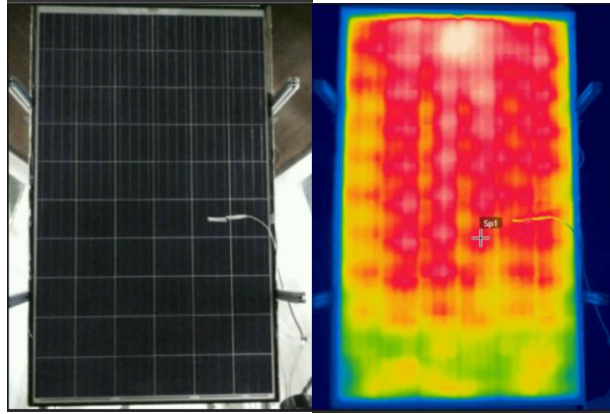


Figure 27 Images taken by FLIR camera; left – normal, right – IR image

To determine the temperature of the PV module, two methods could be employed to obtain this information. The first was completed in FLIR, where a box could be manually drawn over the surface of the PV module to the region of interest that would generate the average PV module temperature for that given formation at a given speed. The example shown below in Figure 28 was taken from back\_full\_run1 at 2m/s, where it can be seen the average temperature within the box is 41.7°C. When processed using the second method, which will be discussed further in detail below in 3.5.2 *MATLAB Processing*, the average temperature is 41.5°C. The first method is constrained by limitations such as an inability to capture temperature variations across the rows of the PV module, hardcoding the numbers singularly, and the potential for error due to the changing region of interest for every image. Despite its quick execution and proximity to true temperature values, the first method exhibits inconsistencies, making using the second method preferable and accurate.

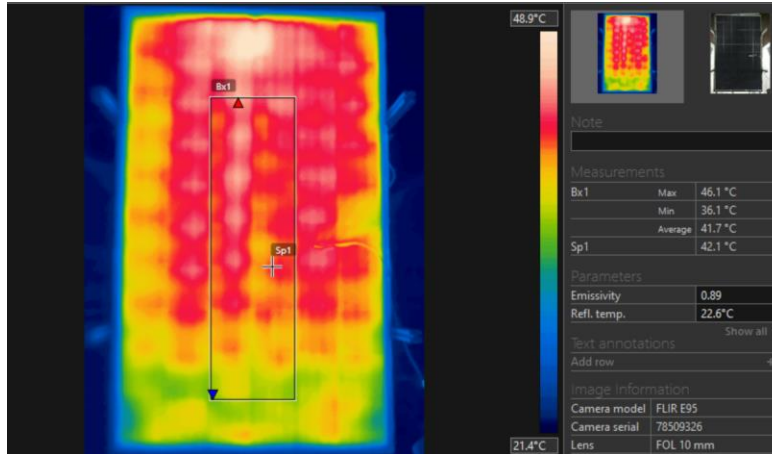


Figure 28 Box method processing

### 3.5.2 MATLAB Processing

The MATLAB code and images throughout processing can be found in Appendix D.

#### Read\_Data.m

Although efforts were made to align the IR camera in the same position, perpendicular to the PV surface, to definitively ensure every image was free from warping/stretching and viewed from the same perspective, the first code applied in MATLAB performed a “de-warping” process to the image. This involved:

- i) Rotating the image by 90°
- ii) Calculating the gradient magnitude and direction, using a “prewitt” gradient operator
- iii) Binarising the image and cropping it to the outline of the PV module
- iv) Finding the corners of the PV module
- v) Dewarp the pixels within the corners and saving the temperature readings as a 380x620 matrix, with its associated parameters into a mat file

#### Delta\_T.m

Once the de-warping process was completed for every image, baseline and VG cases, the next coding sequence comprised of zoning the region of interest and drawing comparisons by:

- i) Identifying the region of interest as shown in Figure 29 as columns  $c_3, c_4$ , and rows  $r_2 - r_9$ . By excluding the outer columns/rows, the potential impacts of inconsistent boundary layers mentioned above, influence from the junction box, lateral conductivity is minimized.

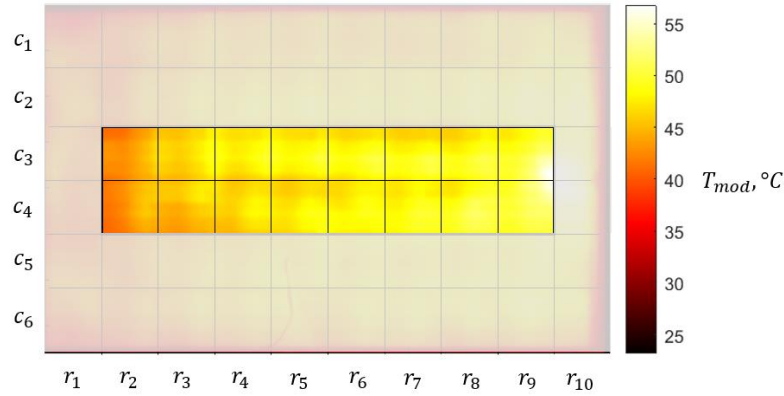


Figure 29 Region of interest zone

- ii) Finding the average of the 2 columns and generating a temperature variable of 8 cells representing the rows along the VG
- iii) Create a temperature fit of the baseline cases for independent wind speeds, using  $T_{mod}$  and  $T_{amb}$ .
- iv) Finding the predicted baseline temperature  $T_{pred}$ , at the same ambient temperature of the VG case under consideration
- v) Obtaining delta T ( $\Delta T$ ) by finding the difference between the predicted temperature and the VG module temperature. For all values greater than zero, this depicted a cooling effect, and all negative values reflected heating.

## 4 Results and Discussion

*The experimental results were produced and gathered initially alongside and under the supervision of Tingyi Zhang for the first half of the year. For the remainder of the year, the results were constructed and gathered independently. All CFD results and CFD figures were provided by Svetlana Tkachenko. All Figures, Tables and Discussions produced in this section are of my own work.*

### 4.1 Characterisation of the Wind Tunnel and Ambient Temperature Considerations

For the experimental phase to be completed with high reproducibility and generate results that were of high accuracy and reliability without transient fluctuations, the stabilisation time of initiating the LWT, and time between adjusting the wind speeds, needed to be found. These timings then formed the experimental basis upon which every subsequent testing was taken under to ensure consistency and stability of results at each speed for each configuration. At first, it was unknown whether a cascading temperature effect from the external ambient environment would drastically affect the laboratory room, and then the temperatures of the LWT. To justify the relative temperature behaviours, the laboratory volume was assumed to be substantially large enough not to experience sudden changes from effects of the external environment. The LWT and the ambient laboratory room were then assessed to form a relationship between the two and identify whether results should be scaled depending on the laboratory's temperatures. Figure 30 shows the



relative temperatures adjusting with the temperature of the day, with the red line depicting the difference and stability of the system.

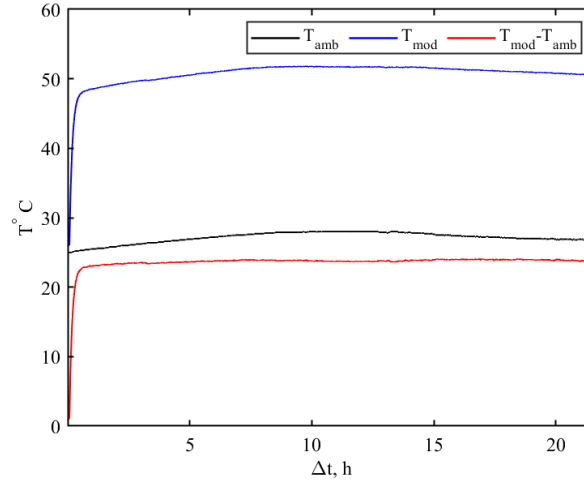


Figure 30 Relative temperature changes of LWT system

Using the information within the Figure 30, the minimum time required for the start-up of the LWT to stabilise to the first speed was found to be approximately 43 minutes. The red line depicts the difference and any fluctuations experienced between the LWT and laboratory room. The gradient of this line after stabilisation was found to have close to a zero gradient, shown below, indicating there is consistent correlation and any incremental change in one directly influences the other.

$$y = 0.02654x + 23.453$$

As this was only completed once, the initiating time was given 1hr 40min – 2hrs as excess to definitively ensure the LWT had reached stability for every formation assessed. This is supported by Zhou et al, where 2hrs was the conclusive time decided for a natural convection case to stabilise within the same space [74].

With the continuous operation of the LWT, the adjustment periods between increasing the wind speeds reduced with increasing speed, with the first stabilisation time between 1-2m/s requiring a minimum of 22 minutes, and 2-3m/s requiring a minimum of 19 minutes. The trends of adjusting the wind speeds from 1m/s through to 3m/s are shown in Figure 31 below, with 1, 2, 3m/s having average temperatures of 23°C, 18.3°C, 15.8°C respectively. Again, to guarantee the temperature within the LWT and of the module had stabilised, a 50 mins period was abided to between speed adjustments before taking IR images. At each speed, an interval of 10-15min was given between thermal images taken to dampen any turbulent effects and produce consistency of results.

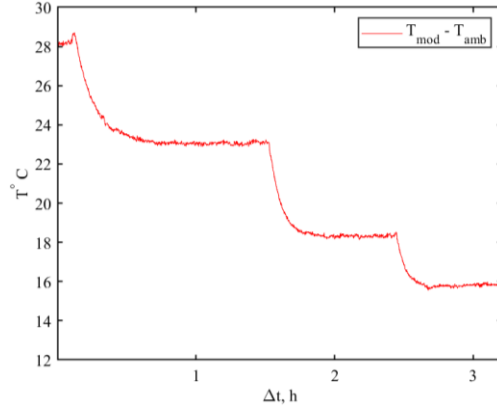


Figure 31 Temperature changes of LWT against different wind speeds

#### 4.2 Baseline Results and Temperature Fits

With the process of result-taking formulated, the next phase required a broad set of baseline results to be the control case for referencing VG cases against. Following on from Literature discussing the usual array formation PV modules are generally installed in, and the use of side panels in the Methodology, the baselines for all speeds and across numerous days were taken using side panels. As ambient temperatures fluctuated significantly across the year, the baselines could not be taken sequentially and were iterated between testing VG cases to produce a broad temperature base for all results to compare against. Because of this staggered data accumulation, the validity of the baseline fits improved throughout the duration of the year. Initially to simplify the segmenting of results to wind speeds alone, the baseline fits were created using the average of the 8 cells from the PV module surface. A linear equation was fitted between the baseline module temperatures and the ambient air temperature at these measurements. This can be found in table blah below, where x denotes the ambient air temperature and y denotes the module temperature. The relationship found for each speed underpinned the process to draw conclusions on the VG effects. Figure 32 below shows the temperature fits for the speeds, where the highest density of results can be seen in the  $< 25^{\circ}\text{C}$  ambient temperature region. A total of 30 baseline cases for each speed were taken across the year, however two of the earlier results were omitted from the following Figure with errors arising from the IR camera changing tilt angle throughout the process.

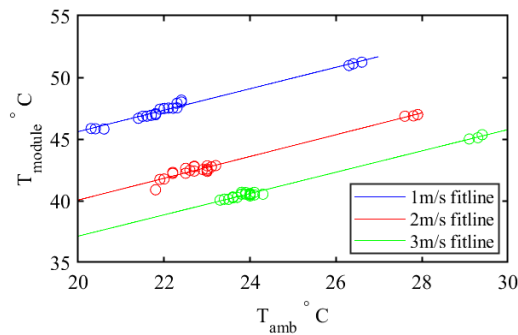


Figure 32 Fitline trends using average surface temperatures

Table 2 Fitline equations for each speed

Speed	Fitted Equation
1m/s	$y = 0.87x + 28.2$
2m/s	$y = 0.883x + 22.39$
3m/s	$y = 0.864x + 19.84$

An alternative method of formulating baseline fits was explored by sectioning the module into rows and creating relationships between each row and the ambient air temperature, generating a total of 24 baseline fits for all speeds. This was considered to check whether any accuracy was impinged in taking the average of the module and by relating an 8-cell variable to an individual ambient temperature. The 8 fits for each speed are shown in Figure 33-35 below.

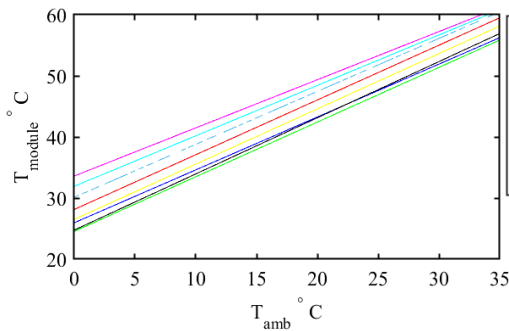


Figure 33 8 row trendlines for 1m/s

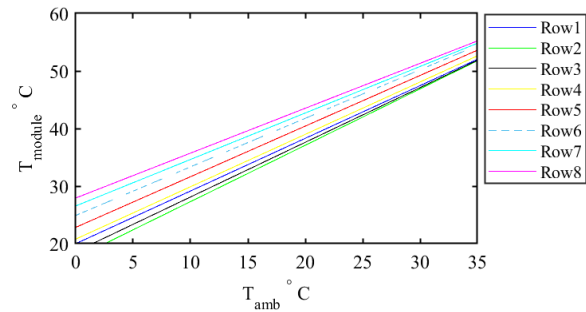


Figure 34 8 row trendlines for 2m/s

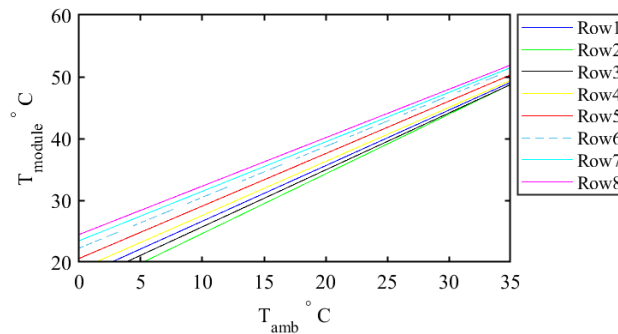


Figure 35 8 row trendlines for 3m/s

Delta T results obtained when comparing the two processes concluded there was no difference between taking the average module temperature and comparing each row individually, meaning the average of all 8 fitlines in each Figure is equal to the equations in Table 2. This process provided more insight into the thermal behaviour of the PV module surface under this particular experimental setup on a row-by-row basis, enabling a clear temperature trend to be formulated of the across the module, shown in Figure 36-38 below ranging from 1m/s to 3m/s. The gradual increase in module temperature from the lower edge to the top of the PV module (from row 1 to 8) was expected with the junction box delivering the heat to the entire module

being located at the upper end of the PV module. What was found to be unusual was the slight increase in module temperature in Row 1 for all speeds.

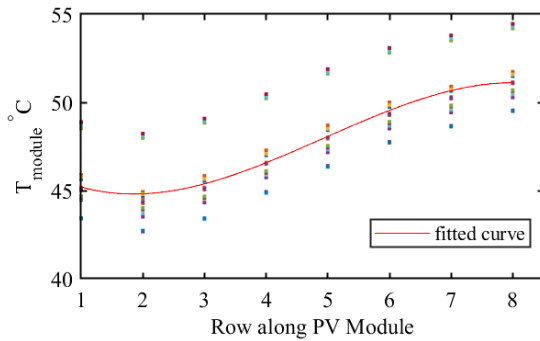


Figure 36 Temperature trend across PV module rows for 1m/s

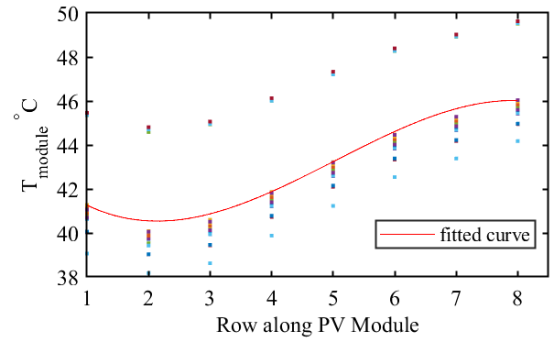


Figure 37 Temperature trend across PV module rows for 2m/s

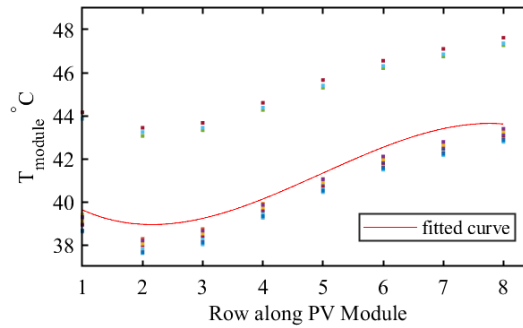


Figure 38 Temperature trend across PV module rows for 3m/s

### 4.3 VG Results

The initial exploration into VG cooling under forced convection considered a concise number of formations and sought to iterate these a number of times to establish a large sample size for each. Below, in Figure 39, shows a graphical representation of how Delta T is obtained, using the 1m/s fitline as an example and plotting a VG data point with its ambient temperature and average module temperature. By scaling the ambient temperatures to equal one another between the baseline and VG case, a direct comparison can be made about the cooling (or heating) effect a VG case has on the PV module, shown with the dashed black line between the “x” and blue line.

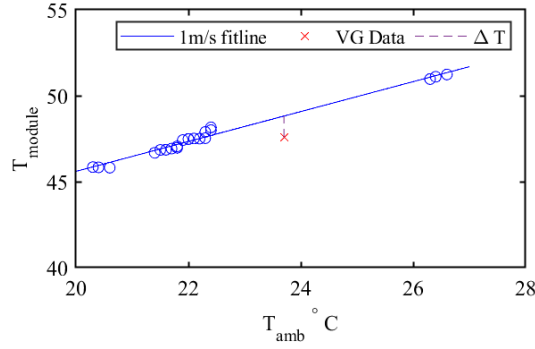


Figure 39 Delta T between baseline and VG case graphically

Following on from discussing the thermal profile across the rows above, the  $\Delta T$  results of all cases were found initially considering rows 2:7 (six rows), in line with the natural convection paper process, and then for comparison, rows 1:8 as per stated in Methodology (8 rows). The average  $\Delta T$  results of each are depicted below in Figure 40 and 41. By considering all the cells, it is clear the trending of each formation assessed is more in align with expected outcome with each case decreasing nearly linearly as speed increases, which will be discussed further later. By reflecting on the temperature curves in Figures 36-38 above, it was evaluated the first and last column does not spike/increase in temperature, which could be expected if the row were heavily impacted by the presence of the junction box within this region. Instead, the curve plateaus for every speed at row 8, underpinning the need to only crop the image one row in from each end of the PV module and maximising the information from the PV module. In lieu of this, the remainder of the analysis considered all 8 rows.

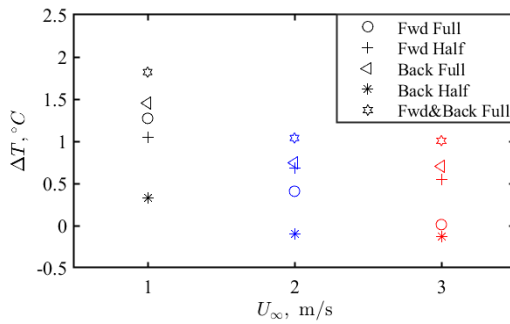


Figure 40 Delta T trend for rows 1:8

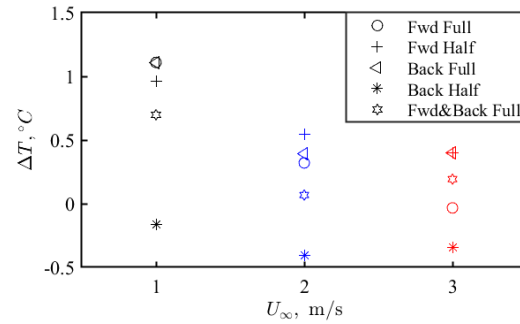


Figure 41 Delta T trend for rows 2:8

#### 4.3.1 Thermal Behaviour Analysis

Relating the standard deviation ( $\sigma$ ) and the sample size ( $N$ ) per case assessed is important to reflect when considering the results gathered. By comparing these, homogeneity of results and robustness, or, reasonings for inconclusive results can be established. The standard deviations and mean values of each formation are shown in Figure 42-46.

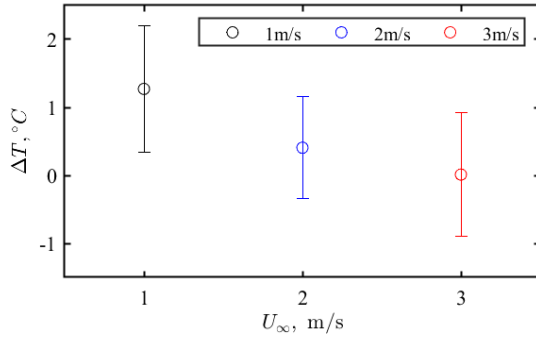


Figure 42 fwd\_full Delta T trend

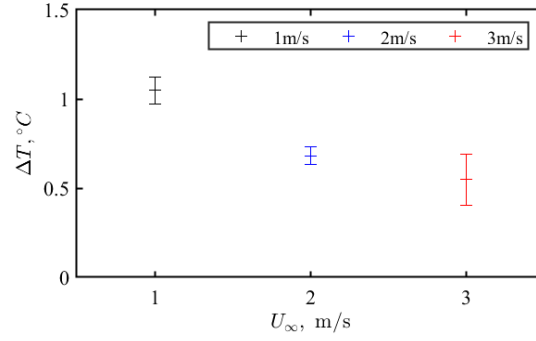


Figure 43 fwd\_half Delta T trend

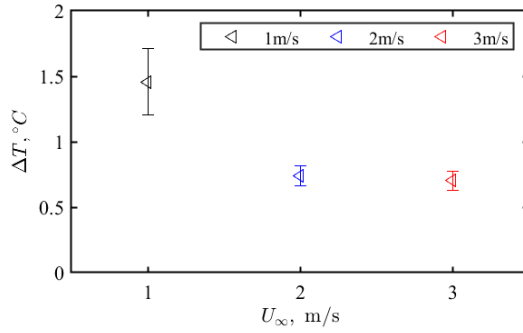


Figure 44 back\_full Delta T trend

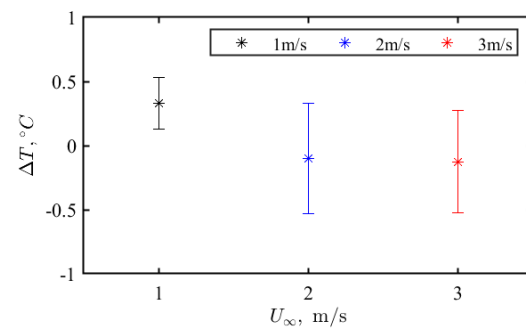


Figure 45 back\_half Delta T trend

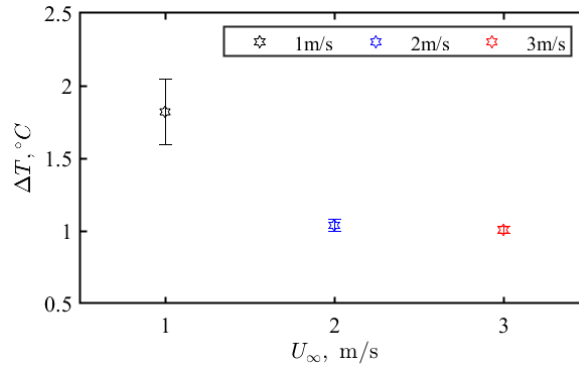


Figure 46 fwdback\_full Delta T trend

The fwd\_full case, seen in Figure 42, had the largest sample size of 10 but interestingly, produced the largest standard deviation of 0.93 at 1m/s. This deviation, however, was the second most consistent across all cases. The most consistent deviation across all speeds was the fwd\_half case, but this could be linked to being a small sample size, taken all on the same day. The fwd\_full case was iterated at varying points throughout the year, due to early discrepancies arising between experimental and simulating results. The large discrepancy in  $\Delta T$  at each speed could be attributed to many reasons; unconscious adjustments made when installing the VGs (human error), slightly varied wind speeds offset from true speeds (as the tunnel

speed would increase slightly with time), a lack of consistency in orientation/formation with VGs becoming unstuck throughout testing, baseline fitline breadth not existing as of yet with only 1 days' worth of baseline testing run around  $\sim 30^{\circ}\text{C}$  (the ambient temperature of when the fwd\_full case was mostly completed). As the outliers of the sample could not be determined with all iterations following the methodology and no obvious errors in data collection known, it can be concluded that to reduce variability in future, results should be taken sequentially, without re-installing VGs along the acrylic surface, per the fwdback\_full case doing so and showing little discrepancy in results at each speed.

Despite the fwd\_full case having high sample size and error, this correlation was not consistent throughout the rest of the results, where the fwdback\_full case had a sample size of 5 and produced the smallest deviation of  $0.0217^{\circ}\text{C}$ , at 3m/s, seen in Figure 46. The smallest sample size was 3 for cases fwd\_half and back\_half. By viewing Figure 43 and 45 for these cases, it can be seen there are no distinct trends between standard deviation size or prominence on any of the speeds.

The absence of any clear pattern between standard deviations and formations assessed necessitates the need to review the experimental procedure and explore deeper the impact sample size has on varying the result distribution, particularly throughout a yearly period of fluctuating seasons. With the potential to obtain a higher volume of results in the future, removing outliers may become possible when each formation has a high resource base to methodically narrow down. It is also a possibility that the intrinsic temperature sensitivity of PV modules may introduce an inherent variability in results that ultimately make forming straightforward conclusions between cases difficult.

A clear trend with all cases when considering the mean was the gradual decrease in cooling effect moving from 1m/s to 3m/s. As the baseline flow, mentioned in blah section, was already categorized as very turbulent, this result could be anticipated with the convective heat transfer coefficient (CHTC) deteriorating with increasing turbulent flow, per Figure 8 in *Literature* section. Every case depicted a distinct leader in maximizing a cooling effect at 1m/s. For all, bar the back\_half case, the introduced turbulence from the presence of VGs showed a capacity to cool the PV module, highlighting the positive impact VG technology in PV modules can make. Table blah in Appendix E shows the precise values of the sample size, mean, median and standard deviations for the Delta T impact for each case and speed.

When directly comparing the full case against the reciprocating half case, the forward full case presented, on average, a slightly worse cooling capability than the half case ( $0.56^{\circ}\text{C}$  vs  $0.76^{\circ}\text{C}$ ). Based on the direction of the oncoming wind with respect to the forward-facing VG, it could be presumed the vertical fill of the

full case stagnated flow more than the half case, bundling the vortices under the VG (Fig blah). This in turn does not direct higher volumes of air onto, or assist in pulling heat away from the PV module surface. When the height of the VG is not as prominent (ie half), this reduces the flow stagnation effect whilst pushing air upwards when passing by the lip of the VG.

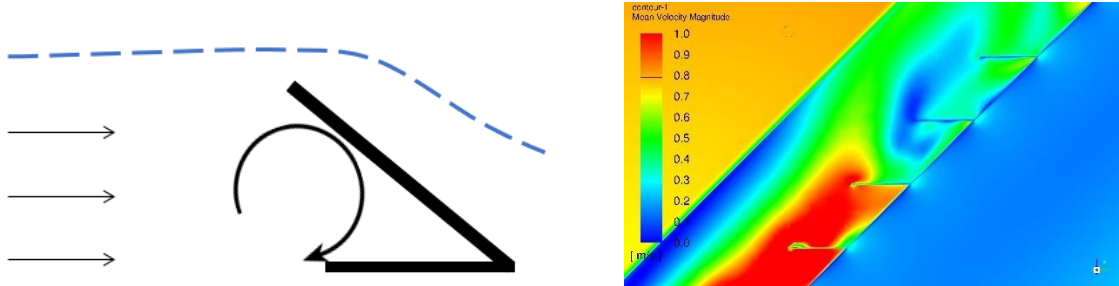


Figure 47 Vortex creation against forward facing VG; left – diagram, right – CFD

In discussing the vortex creation with the orientation of the VGs, it can hence be expected that the back\_full case would have a greater cooling impact than the fwd\_full case with the vortices anticipated to develop as shown in Figure 47. When placed at close intervals down the length of the acrylic board, airflow is constantly encouraged upwards to the VG module without hindering the velocity of the flow. Because of this, the back\_full case produced significantly more cooling than the back\_half case, with the extended length of the VG influencing a higher volume of air upwards, and as well as enabling it to reach into the thermal boundary layer on the underside of the PV module and increase mixing.

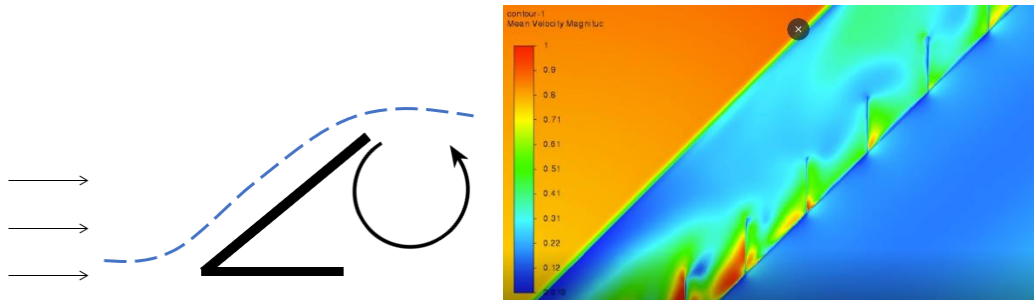


Figure 48 Vortex creation against backwards facing VG; left – diagram, right – CFD

The back\_half case lacked the reach (height) to be able to significantly disrupt the thermal boundary layer on the underside of the PV module, or the aerodynamic strength to manipulate the adjacent flow field towards it, subduing its capacity to promote cooling. When flow was slightly stagnated by the production of vortices under the VG for the fwd\_half case, this centripetal bundling of air influences the adjacent air to accommodate for this space, and move over the VG higher than the back\_half would promote. This is shown above in Figure 48. For these reasons, the fwd\_half case had better cooling potential, for every speed, than the back\_half case.



The formation which most successfully cooled the PV module was the fwdback\_full case with a  $\Delta T$  of  $1.82^{\circ}\text{C}$  at  $1\text{m/s}$  with a  $\sigma$  of  $0.2257$ , where a blend of both forward and backward facing VGs were installed. This can be attributed to the high fill ratio in the spanwise direction ( $P_x/W$ ), directing a higher volume of air towards the PV module, supported by results obtained by Bittagopal Mondal et al. when increasing the density of VGs [72]. The elevated  $\Delta T$  throughout all speeds is made more interesting by the poor result the fwd\_full case produced alone at  $2\text{m/s}$  and  $3\text{m/s}$ .

The next natural progression of this formation would be to investigate whether a combination of fwd\_half and back\_full would prove even more effective at cooling, based upon the higher cooling impact the fwd\_half case had. Beyond this, the highly favorable results in cooling by increasing the spanwise density of VGs should be investigated by increasing the control size of VGs from  $66$ , as well as experimenting with adjusting the width of VGs from  $4\text{cm}$  wide. With the aligned formation implemented in all test cases, it would prove beneficial to understand whether using staggered formations down the length of the acrylic board would manipulate a higher volume of air flowing through the gap upwards to the PV module, or whether this would block the generation of vortex channels down the length of the acrylic board. Figure 49 depicts an example of increasing the spanwise density of VGs.

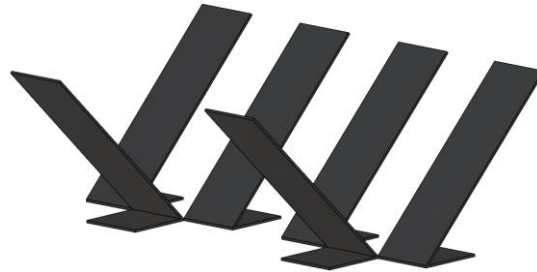


Figure 49 Example of future formations to assess

#### 4.4 Experimental against Simulation

A numerical model was created alongside the experimental testing phase to virtually model the experiment into a simulating environment. This was completed to ascertain whether, like blah study, a direct linear trend, likely offset vertically, could be generated to predict future experimentation in the same LWT. In the same way that the experimental baseline and VG cases were constructed and then compared, the CFD modelling within ANSYS Fluent R1 followed the same method. To computationally situate the entire PV module configuration into a theoretical LWT, the PV module was suspended  $0.5\text{m}$  from the floor, inside a hexagonal cross-section meshed tunnel. Although the length of the Large Test Section is  $4.5\text{m}$  long, the virtual length of this same space was set with a length of  $20\text{m}$  to avoid numerical errors. The sample size of the CFD modelling was limited to 1 iteration using an ambient temperature of  $25^{\circ}\text{C}$ . Figure 50-53

show the trends of the CFD results (filled) against the experimental values. The fwdback\_full case has not yet been produced as a numerical model and is omitted from comparison.

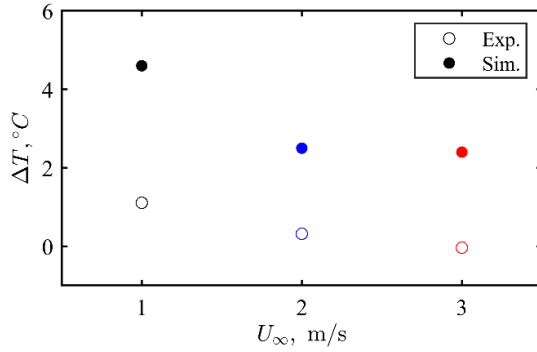


Figure 50 fwd\_full Delta T comparison

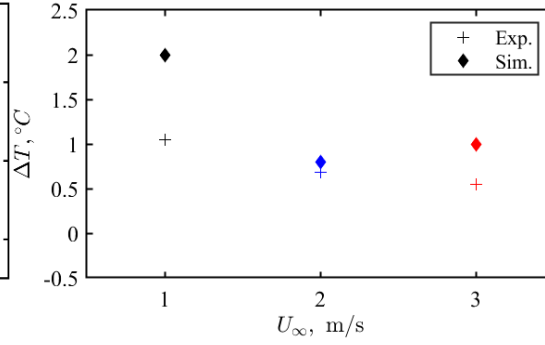


Figure 51 fwd\_half Delta T comparison

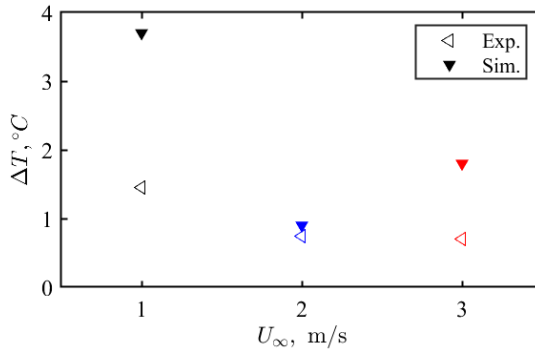


Figure 52 back\_full Delta T comparison

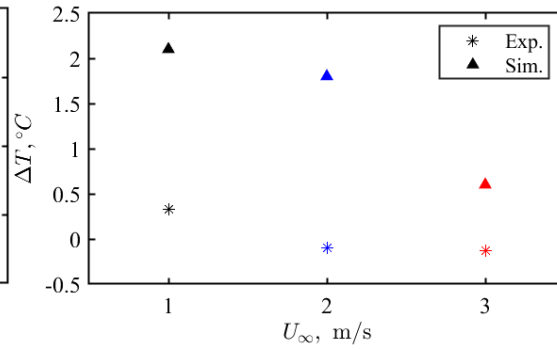


Figure 53 back\_half Delta T comparison

The case which produced the closest trend, offset by a vertical distance, was the fwd\_full formation. Overall, the CFD modelling produced results that were inconclusive and showed no consistency or trends between any of the variables. This outcome removes the credibility to validate the experimental results against, and requires a critical evaluation on how the PV module was situated into the virtual environment concerning the boundary conditions, turbulent flow modelling and fluid flow assumptions, dimensions, meshing and convergence of results. As the CFD modelling has only been completed once at a set ambient temperature, iterations parametrizing the ambient temperature will provide a more extensive database to compare VG cases against. In lieu of the CFD outcome, the experimental results processed on my behalf were validated against independent and unbiased processing completed by Tingyi Zhang.

#### 4.5 Design Modifications to Experimental Frame

With limited time and constrained financial resources, the opportunity to completely redesign, build and install, whilst simultaneously complete testing of baseline and VG formations, was limited to prioritizing the frame's base. The main benefit the base was to provide was reducing the time expense associated with

changing the formation of VGs and installation method. The method used throughout the thesis, using wooden strips and lots of sticky tape, had issues arising from inconsistent placements/spacings between VGs when installed, Fig blah, poor resilience against extended testing, and when removing the wooden strips, lead to fractures and breaks in the lengths which required more time to repair these. The installation required another person to be present and the time to complete a change of formation generally took at least an hour, which for an experiment which already requires at least 5 hours of a day to conduct the experiment, was very detrimental to time efficiency.

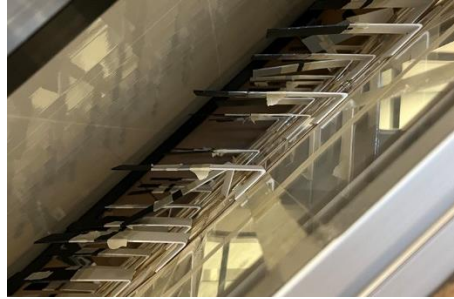


*Figure 54 Photo of misaligned VGs and collapsed array*

The new base was chosen to be built and installed in time for fwdback\_full case, where modularity and alternating orientation of the VGs was required. The initial design concept to achieve this first considered channel indents where the VGs could snugly be fitted into the gap at any horizontal location, discovering which length would make this possible (at 38.5mm). However, the physical integration of this design into the board was difficult to achieve as distances were compromised with flexing strips. Instead, 3mm grooves at a depth of 5mm were routed along the width of the board and the VGs affixed using strips to provide the gripping action of the first design (Figure 55 left). This was further improved by creating L-bracket shapes (orange) from acrylic (Figure 55 right) and the grooves filled to ensure the board was smooth (without rungs) like the acrylic board.



*Figure 55 Designs to hold VGs in place; left - rungs, right - L-shapes*

For any subsequent testing to be completed, the baseline effect of the designed wooden base needed to be compared with the acrylic baselines to assess whether there was any cooling or heating differences occurring. This is shown in Figure 56 below, where unfortunately there were discrepancies for all cases showing a cooling effect, likely a result of the grooves and/or the surface roughness of the wood. If the wooden base was to be used to create the fwd\_full\_case, all the experiments to date would have to be repeated, as well as the baselines, to then compare the formations cooling/heating potentials again. With more baselines required for the acrylic board and the limited time, the wooden base was abandoned for the fwdback\_full case. The VGs were installed after the acrylic baseline test was done using only sticky tape.

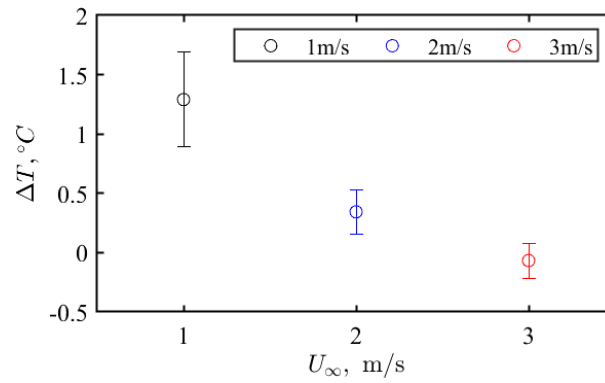


Figure 56 Cooling effect wooden board produce compared to the acrylic baselines

## 5 Conclusions and Future Work

The objective of this thesis was to experimentally explore the cooling capability VGs had on PV modules, whilst experiencing forced convection. Chapter 2 evaluated gaps in literature for passive and active cooling methods, finding that the impact of incorporating rectangular VGs on an inclined roofing layer under a PV system had not yet been discovered. Vortex generators were chosen as the focus of promoting cooling for their simplicity, affordability, and strong aerodynamic ability.

Experiments were conducted in the LWT in the UNSW Laboratory to experimentally situate a model of a PV system experiencing overheating from an excess of thermal energy present. This was achieved using a Power Supply to deliver  $900\text{W/m}^2$  to the PV module by means of a junction box. To ensure all results were stable, the LWT was characterised to determine the minimum time required to stabilise, as well as the relative temperature impact of the adjacent environment. IR imaging and thermocouples were the primary means of obtaining data on the thermal profiles that developed on and around the PV module. Baselines were formed to draw comparisons against and establish the direct causal effect of implementing VGs into this system. The results of the VG cases are as follows:

- i) All VG formations, save the back\_half case, facilitated cooling in the PV module to some extent, with the most effective cooling observed at a speed of  $1\text{m/s}$ .
- ii) The fwdback\_full produced the most cooling with a  $\Delta T$  of  $1.82^\circ\text{C}$ . This result is likely from an increase of the  $P_x/W$  fill ratio and should be investigated further to determine the optimal ratio. This could increase module lifespan by around 15%.
- iii) The  $\Delta T$  effect when considering the  $H/G$  fill ratio was dependent on VG orientation, where the back\_full disturbed the boundary layer more than the back\_half case, but the fwd\_full on average produced less cooling than the fwd\_half, with significantly more variation in results.
- iv) The back\_full case encouraged a higher level of cooling in the PV module than the fwd\_full case, with a lower overall flow rate developing in the latter.

A new wooden board to replace the acrylic roof, for mounting the VGs onto, was created, optimizing the time efficiency for installing rectangular VGs. The wooden board depicted cooling compared to the acrylic board and with the limited time, was not explored further.

With VGs presenting a novel method of facilitating cooling in PV module systems under forced convection, there are numerous avenues to deepen understandings of PV module response to cooling, whilst uncovering the cooling extent that can be achieved by using VGs. Future work that could be completed is detailed below.

- The variation in results should be investigated to uncover the root cause by considering whether consistent sample sizes and testing throughout various points of the year improves or degrades result quality.
- As the results of this report could not be validated against CFD modelling, both the experimental design and CFD simulation should be reviewed and eventually complement the others' trends. The realistic heating over a PV module should be validated on a large-scale outdoor system to discern the heating profile a PV module experiences under the Sun, and parametrization of row considerations should be conducted to conclude where the boundary effects are negligible. Analyses using Particle Image Velocimetry (PIV) would also build upon the findings of this report, offering experimental validation for the discussed flow features. This is particularly pertinent for future investigations involving vortex generators.
- Optimization for the spacings and shapes of VGs should be tailored to forced convection conditions and could consider ways to generate strong VGs without impeding flow rates.

## References

- [1] US EPA, "Global Greenhouse Gas Emissions Data," 15 February 2023. [Online]. Available: <https://www.epa.gov/ghgemissions/global-greenhouse-gas-emissions-data#:~:text=Since%201970%2C%20CO2%20emissions,been%20the%20second%2Dlargest%20contributors.> [Accessed February 2023].
- [2] IEA, "Russia's War on Ukraine," IEA, Feb 2023. [Online]. Available: <https://www.iea.org/topics/russias-war-on-ukraine>. [Accessed March 2023].
- [3] BP p.l.c., "Statistical Review of World Energy," BP p.l.c., London, UK, 2020.
- [4] D. L. Chandler, "Shining brightly," Massachusetts Institute of Technology, 26 October 2011. [Online]. Available: <https://news.mit.edu/2011/energy-scale-part3-1026#:~:text=A%20total%20of%20173%2C000%20terawatts,energy%20strikes%20the%20Earth%20continuously.> [Accessed February 2023].
- [5] IEA, "SDG7: Data and Projections - Access to electricity," IEA, 2023. [Online]. Available: <https://www.iea.org/reports/sdg7-data-and-projections/access-to-electricity>. [Accessed June 2023].
- [6] Center for Sustainable Systems, "Photovoltaic Energy Factsheet," University of Michigan, 2023. [Online]. Available: <https://css.umich.edu/publications/factsheets/energy/photovoltaic-energy-factsheet#:~:text=Though%20most%20commercial%20panels%20have,cells%20with%20efficiencies%20approaching%2050%25.&text=Assuming%20intermediate%20efficiency%2C%20PV%20covering,electrici.> [Accessed February 2023].
- [7] L. C. a. G. F. Feng Shan, "Dynamic performances modeling of a photovoltaic–thermal collector with water heating in buildings," *Energy and Buildings*, vol. 66, 2013.
- [8] A. Zewe, "To improve solar and other clean energy tech, look beyond hardware," MIT News, August 2023. [Online]. Available: <https://news.mit.edu/2023/improving-solar-looking-beyond-hardware-0817>. [Accessed September 2023].
- [9] Geoscience Australia, "Solar Energy," Geoscience Australia, 7 June 2023. [Online]. Available: <https://www.ga.gov.au/scientific-topics/energy/resources/other-renewable-energy-resources/solar-energy>. [Accessed September 2023].

- [10] ARENA, "Solar energy," Australian Government, 15 November 2023. [Online]. Available: <https://arena.gov.au/renewable-energy/solar/>. [Accessed November 2023].
- [11] IEA, "Renewable power's growth is being turbocharged as countries seek to strengthen energy security," IEA, 06 December 2022. [Online]. Available: <https://www.iea.org/news/renewable-power-s-growth-is-being-turbocharged-as-countries-seek-to-strengthen-energy-security>. [Accessed March 2023].
- [12] P. Bojek, "Solar PV," IEA, 11 July 2023. [Online]. Available: <https://www.iea.org/energy-system/renewables/solar-pv>. [Accessed August 2023].
- [13] M. Taylor, "Falling Costs Drive Strong Demand for Australia's Residential Solar PV," IRENA, 20 May 2022. [Online]. Available: <https://www.irena.org/News/expertinsights/2022/May/Falling-costs-drive-strong-demand-for-Australias-residential-solar-PV#:~:text=Cost%20reductions%20have%20changed%20the,%C2%A2%20per%20kWh%20in%202020..> [Accessed August 2023].
- [14] K. Kumar, "A History of the Solar Cell, in Patents," 27 April 2020. [Online]. Available: <https://www.finnegan.com/en/insights/articles/a-history-of-the-solar-cell-in-patents.html#:~:text=In%201954%2C%20Bell%20Labs'%20Daryl,several%20hours%20of%20a%20day.&text=Their%20patent%2C%20US%20patent%20no%202%2C780%2C765%2C%20issued%20in%201957>. [Accessed February 2023].
- [15] ACS Chemistry for Life, "How a Solar Cell Works," 2023. [Online]. Available: <https://www.acs.org/education/resources/highschool/chemmatters/past-issues/archive-2013-2014/how-a-solar-cell-works.html>. [Accessed February 2023].
- [16] Office of Energy Efficiency & Renewable Energy, "Solar Photovoltaic Cell Basics," [Online]. Available: <https://www.energy.gov/eere/solar/solar-photovoltaic-cell-basics#:~:text=Silicon,of%20the%20modules%20sold%20today>. [Accessed February 2023].
- [17] R. P. D. B. S.W. Glunz, "1.16 - Crystalline Silicon Solar Cells: State-of-the-Art and Future Developments," 10 May 2012. [Online]. Available: <https://www.sciencedirect.com/science/article/abs/pii/B9780080878720001177>. [Accessed February 2023].
- [18] NREL Transforming Energy, "News Release: NREL Creates Highest Efficiency 1-Sun Solar Cell," 18 May 2022. [Online]. Available: <https://www.nrel.gov/news/press/2022/nrel-creates-highest-efficiency-1-sun-solar-cell.html>. [Accessed February 2023].



- [19] EIA, "Solar explained: Solar thermal power plants," U.S. Energy Information Administration, 15 April 2022. [Online]. Available: <https://www.eia.gov/energyexplained/solar/solar-thermal-power-plants.php#:~:text=Solar%20thermal%20power%20systems%20use%20concentrated%20solar%20energy&text=The%20steam%20is%20converted%20into,changes%20position%20in%20the%20sky..> [Accessed June 2023].
- [20] P. L. M. H. H.G. Teo, "An active cooling system for photovoltaic modules," 4 February 2011. [Online]. Available: <https://pdf.sciencedirectassets.com/271429/1-s2.0-S0306261911X00119/1-s2.0-S0306261911000201/main.pdf?X-Amz-Security-Token=IQoJb3JpZ2luX2VjEC4aCXVzLWVhc3QtMSJHMEUCICju9ryHCeXqprKVGie uTgbD%2FYi52y%2BK4uvl50%2BiNCpeAiEAqNEWXXUba6X1A4%2Bx3NrbzjtjcgHM5FljKHtI.> [Accessed February 2023].
- [21] S. Kalogirou, "Solar Energy Engineering," in *Processes and Systems*, Academic Press, 2009, pp. 483-491.
- [22] A. Zhao, "Silicon Solar Cells," Stanford University, 13 November 2015. [Online]. Available: Silicon Solar Cells. [Accessed June 2023].
- [23] I. Sheik Md Kazi Nazrul and . A. Al Jumlat, "New Design of Solar Photovoltaic and Thermal Hybrid System for Performance Improvement of Solar Photovoltaic," *International Journal of Photoenergy*, 2020.
- [24] B. R. Sutherland, "Solar Materials Find Their Band Gap," 20 May 2020. [Online]. Available: <https://www.sciencedirect.com/science/article/pii/S2542435120301847>. [Accessed February 2023].
- [25] A. K. A. P. R. C. S. P. Himanshu Tyagi, *Advances in Solar Energy Research*, Springer, 2019.
- [26] S. P. C. L. D. C. Rodolphe Vaillon 1, "Solar Cells Operating under Thermal Stress," 2 December 2020. [Online]. Available: <https://www.sciencedirect.com/science/article/pii/S2666386420302897>. [Accessed February 2023].
- [27] A. Zanatta, "The Shockley–Queisser limit and the conversion efficiency of silicon-based solar cells," in *Results in Optics*, Brazil, 2022, pp. 100-320.
- [28] D. J. H. F. N. J. W. Emeka H. Amalu, "Thermo-mechanical deformation degradation of crystalline silicon photovoltaic (c-Si PV) module in operation," 28 November 2017. [Online]. Available:

- <https://www.sciencedirect.com/science/article/abs/pii/S1350630717311834>. [Accessed March 2023].
- [29] G. C. A. F. F. Arpino, "Experimental and numerical assessment of photovoltaic collectors performance dependence on frame size and installation technique," 27 May 2015. [Online]. Available: <https://www.sciencedirect.com/science/article/abs/pii/S0038092X15002297>. [Accessed February 2023].
- [30] D. P. Claudio Ferrara, "Why Do PV Modules Fail?," 30 March 2012. [Online]. Available: [https://pdf.sciencedirectassets.com/277910/1-s2.0-S1876610212X00031/1-s2.0-S1876610212003827/main.pdf?X-Amz-Security-Token=IQoJb3JpZ2luX2VjEPz%2F%2F%2F%2F%2F%2F%2F%2F%2F%2FwEaCXVzLWVhc3QtMSJIMEYCIQDrNvlFLB5OJ2irdisIWqwdDNoyQkRsZ0Hv%2BM6OMl1PbgIhANADgpgwYv](https://pdf.sciencedirectassets.com/277910/1-s2.0-S1876610212X00031/1-s2.0-S1876610212003827/main.pdf?X-Amz-Security-Token=IQoJb3JpZ2luX2VjEPz%2F%2F%2F%2F%2F%2F%2F%2F%2F%2F%2FwEaCXVzLWVhc3QtMSJIMEYCIQDrNvlFLB5OJ2irdisIWqwdDNoyQkRsZ0Hv%2BM6OMl1PbgIhANADgpgwYv). [Accessed February 2023].
- [31] Z. Z. ., C. J. Shifeng Denga, "Research on hot spot risk for high-efficiency solar module," 20 April 2017. [Online]. Available: <https://pdf.sciencedirectassets.com/277910/1-s2.0-S1876610217X00283/1-s2.0-S1876610217344909/main.pdf?X-Amz-Security-Token=IQoJb3JpZ2luX2VjEGEaCXVzLWVhc3QtMSJHMEUCIBY3MR59QM4g2I%2BXQdpXhTWhBKWFzZuXoaBLoRT%2FQa68AiEAqAaZI1cOP3w%2BIr2EYzc2k76r6IB0Oy1lgIFKuO>. [Accessed February 2023].
- [32] F. G.-. Č. I. M.-K. A. P. S. Nižetić a, "https://www.sciencedirect.com/science/article/abs/pii/S0360544216307228," 26 May 2016. [Online]. Available: Experimental and numerical investigation of a backside convective cooling mechanism on photovoltaic panels. [Accessed February 2023].
- [33] R. V. & M. A. G. Thermal Issues in Photovoltaics and Existing Solutions Olivier Dupré, "Thermal Issues in Photovoltaics and Existing Solutions," 3 December 2016. [Online]. Available: [https://link.springer.com/chapter/10.1007/978-3-319-49457-9\\_1](https://link.springer.com/chapter/10.1007/978-3-319-49457-9_1). [Accessed March 2023].
- [34] D. Herring, "Climate Change: Global Temperature Projections," 6 March 2012. [Online]. Available: <https://www.climate.gov/news-features/understanding-climate/climate-change-global-temperature-projections#:~:text=Results%20from%20a%20wide%20range,2100%20than%20it%20is%20today>. [Accessed February 2023].
- [35] D. V. Nadarajah Kannan, "Solar energy for future world: - A review," May 2016. [Online]. Available: <https://www.sciencedirect.com/science/article/pii/S1364032116301320>. [Accessed February 2023].

- [36] ShopSolar, "What Wavelength Do Solar Panels Use?," ShopSolar, 2023. [Online]. Available: <https://shopsolkits.com/blogs/learning-center/what-wavelength-do-solar-panels-use>. [Accessed 2023].
- [37] Oregon University, "Photons into Electrons: photovoltaic Devices," Oregon University, 2003. [Online]. Available: <https://darkwing.uoregon.edu/~stanm/phys162w2006%20phys162s2003/PHYS162/solarelectric/SolarElectricity.html>. [Accessed 2023].
- [38] A. J. G. Yunus A. Cengel, "Heat and mass transfer: Fundamentals and applications," New York, NY, McGraw-Hill Professional, 2023.
- [39] S. B. Christiana Honsberg, "Heat Loss in PV Modules," [Online]. Available: <https://www.pveducation.org/pvcdrom/modules-and-arrays/heat-loss-in-pv-modules>. [Accessed February 2023].
- [40] K. S. A. S. E. S. I. K. Pushpendu Dwivedi a, "Advanced cooling techniques of P.V. modules: A state of art," 3 June 2020. [Online]. Available: <https://www.sciencedirect.com/science/article/pii/S2214157X19305416>. [Accessed March 2023].
- [41] A. J. G. YUNUS A. ÇENGEL, Heat and Mass Transfer; Fundamentals and Applications, New York: McGraw-Hill Education, 2015.
- [42] B. P. G Gunasegarane, "Dynamics of line plumes on horizontal surfaces in turbulent convection," July 2013. [Online]. Available: <https://arxiv.org/pdf/1307.1236.pdf>. [Accessed March 2023].
- [43] J. T. ., G. H. J. P. E. Abbasi Shavazi, "Convection Heat Transfer from an Inclined Narrow Flat Plate with Uniform Flux Boundary Conditions," 10 December 2018. [Online]. Available: [https://people.eng.unimelb.edu.au/imarusic/proceedings/21/Contribution\\_739\\_final.pdf](https://people.eng.unimelb.edu.au/imarusic/proceedings/21/Contribution_739_final.pdf). [Accessed March 2023].
- [44] D. H. G. A. D. M. R. J. Kind, "Convective Heat Losses From Flat-Plate Solar Collectors in Turbulent Winds," February 1983. [Online]. Available: <https://doi.org/10.1115/1.3266350>. [Accessed March 2023].
- [45] L. Wen, "An Investigation of the Effect of Wind Cooling on Photovoltaic Arrays," March 1982. [Online]. Available: <https://ntrs.nasa.gov/api/citations/19820023899/downloads/19820023899.pdf>. [Accessed March 2023].

- [46] D. Ting, "Chapter 16 - Forced convection," in *Thermofluids From Nature to Engineering*, Academic Press, 2022, pp. 319-356.
- [47] O. Z. A. Almuwailhi, "Investigating the cooling of solar photovoltaic modules under the conditions of Riyadh," 15 March 2021. [Online]. Available: <https://www.sciencedirect.com/science/article/pii/S1018363921000453#:~:text=For%20cold%20regions%2C%20PV%20modules,and%20efficiency%20of%20PV%20modules.> [Accessed March 2023].
- [48] T. W. A. Akbarzadeh, "Heat pipe-based cooling systems for photovoltaic cells under concentrated solar radiation," 16 December 1999. [Online]. Available: [https://www.sciencedirect.com/science/article/pii/S1359431195000123?ref=pdf\\_download&fr=RR-2&rr=7bcbcb6accd8a96e](https://www.sciencedirect.com/science/article/pii/S1359431195000123?ref=pdf_download&fr=RR-2&rr=7bcbcb6accd8a96e). [Accessed March 2023].
- [49] H. G. Ram Kumar Agarwal, "Study of a photovoltaic-thermal system—Thermosyphonic solar water heater combined with solar cells," in *Energy Conversion and Management*, New Delhi, Hauz Khas, 1994, pp. 605-620.
- [50] A. M. K. S. H. J. A. F. A. I. A.M. Elbreki a b, "Experimental and economic analysis of passive cooling PV module using fins and planar reflector," 1 December 2020. [Online]. Available: <https://www.sciencedirect.com/science/article/pii/S2214157X20305438>. [Accessed February 2021].
- [51] M. R. S. Kim Trapani, "A review of floating photovoltaic installations: 2007–2013," January 2017. [Online]. Available: [https://www.researchgate.net/publication/260410944\\_A\\_review\\_of\\_floating\\_photovoltaic\\_installations\\_2007-2013](https://www.researchgate.net/publication/260410944_A_review_of_floating_photovoltaic_installations_2007-2013). [Accessed March 2023].
- [52] P. R.-C. G. T. P. S. M. Rosa-Clot, "Submerged photovoltaic solar panel: SP2," 18 October 2009. [Online]. Available: <https://www.sciencedirect.com/science/article/pii/S0960148109004492>. [Accessed March 2023].
- [53] S. Krauter, "Increased electrical yield via water flow over the front of photovoltaic panels," May 2004. [Online]. Available: [https://www.researchgate.net/publication/228404444\\_Increased\\_electrical\\_yield\\_via\\_water\\_flow\\_over\\_the\\_front\\_of\\_photovoltaic\\_panels](https://www.researchgate.net/publication/228404444_Increased_electrical_yield_via_water_flow_over_the_front_of_photovoltaic_panels). [Accessed March 2023].
- [54] M. B. Saad Odeh, "Improving Photovoltaic Module Efficiency Using Water Cooling," May 2009. [Online]. Available: [https://www.researchgate.net/publication/233002128\\_Improving\\_Photovoltaic\\_Module\\_Efficiency\\_Using\\_Water\\_Cooling](https://www.researchgate.net/publication/233002128_Improving_Photovoltaic_Module_Efficiency_Using_Water_Cooling). [Accessed March 2023].

- [55] W. G. R. F. Krzysztof Sornek, "Development and Tests of the Water Cooling System Dedicated to Photovoltaic Panels," August 2022. [Online]. Available: [https://www.researchgate.net/publication/362698627\\_Development\\_and\\_Tests\\_of\\_the\\_Water\\_Cooling\\_System\\_Dedicated\\_to\\_Photovoltaic\\_Panels](https://www.researchgate.net/publication/362698627_Development_and_Tests_of_the_Water_Cooling_System_Dedicated_to_Photovoltaic_Panels). [Accessed March 2023].
- [56] S. A. Salaudeen, "Investigation on the performance and environmental impact of a latent heat thermal energy storage system," 2018. [Online]. Available: <https://www.sciencedirect.com/science/article/pii/S1018363917301873>. [Accessed March 2023].
- [57] G. JR, "Optimization of Air Gap Required Below Solar PV Modules, Mounted on Metal Sheet roof-tops, through Thermal Analysis and Experimental Verification.," International Journal of Innovative Research in Science, Engineering and Technology, Bengaluru, 2017.
- [58] M. I. Y. M. I. A.R. Amelia, "Cooling on photovoltaic panel using forced air convection induced by DC fan," April 2016. [Online]. Available: [https://www.researchgate.net/publication/309769559\\_Cooling\\_on\\_photovoltaic\\_panel\\_using\\_forced\\_air\\_convection\\_induced\\_by\\_DC\\_fan](https://www.researchgate.net/publication/309769559_Cooling_on_photovoltaic_panel_using_forced_air_convection_induced_by_DC_fan). [Accessed March 2023].
- [59] T. N. M. S. P. Y. Y. Tripanagnostopoulos, "Hybrid photovoltaic/thermal solar systems," *Solar Energy*, vol. 72, no. 3, pp. 217-234, 2022.
- [60] A. A. Hegazy, "Comparative study of the performances of four photovoltaic/thermal solar air collectors," *Energy Conversion and Management*, vol. 41, no. 8, pp. 861-881, 2000.
- [61] K. Forster, "How do Vortex Generators Work?," Youtube, 2 July 2014. [Online]. Available: [https://www.youtube.com/watch?v=9Whd\\_KnsLKE&ab\\_channel=KYLE.ENGINEERS](https://www.youtube.com/watch?v=9Whd_KnsLKE&ab_channel=KYLE.ENGINEERS). [Accessed March 2023].
- [62] R. K. Shah and A. M. Jacobi, "Heat Transfer Surface Enhancement through the Use of Longitudinal Vortices: A Review of Recent Progress," in *Experimental Thermal and Fluid Science*, ELSEVIER, 1995, pp. 295-309.
- [63] M. Fiebig, "Vortices, Generators and Heat Transfer," 14 February 2008. [Online]. Available: <https://www.sciencedirect.com/science/article/pii/S0263876298716284>. [Accessed March 2023].
- [64] N. M. M. F. St. Tiggelbeck, "Experimental investigations of heat transfer enhancement and flow losses in a channel with double rows of longitudinal vortex generators," *International Journal of Heat and Mass Transfer*, vol. 36, no. 9, pp. 2327-2337, 1993.
- [65] L. D. Ahmad Sohankar, "EFFECT OF INCLINED VORTEX GENERATORS ON HEAT TRANSFER ENHANCEMENT IN A THREE-DIMENSIONAL CHANNEL," in *Numerical Heat Transfer, Part A: Applications*, Taylor & Francis, 2001, pp. 433-448.

- [66] Q. Y. Guobing Zhou, "Experimental investigations of thermal and flow characteristics of curved trapezoidal winglet type vortex generators," 20 November 2011. [Online]. Available: <https://www.sciencedirect.com/science/article/pii/S1359431111006521>. [Accessed March 2023].
- [67] M. Fiebig, "Embedded vortices in internal flow: heat transfer and pressure loss enhancement," 27 December 1999. [Online]. Available: <https://www.sciencedirect.com/science/article/pii/0142727X9500043P>. [Accessed March 2023].
- [68] P. K. N. M. S. T. Martin Fiebig, "Heat transfer enhancement and drag by longitudinal vortex generators in channel flow," *Experimental Thermal and Fluid Science*, vol. 4, no. 1, pp. 103-114, 1991.
- [69] K. T. D. F. K. N. G. Biswas, "Numerical and experimental determination of flow structure and heat transfer effects of longitudinal vortices in a channel flow," 17 February 1999. [Online]. Available: <https://www.sciencedirect.com/science/article/abs/pii/0017931095003983>. [Accessed March 2023].
- [70] C. H. S. R. D. B. T. L. Assadour Khanjian, "Effect of the angle of attack of a rectangular wing on the heat transfer enhancement in channel flow at low Reynolds number," Springer-Verlag , Germany, 2017.
- [71] P. E. S.V. Garimella, "Enhancement of single phase convective heat transfer from protruding elements using vortex generators," 27 February 2003. [Online]. Available: <https://www.sciencedirect.com/science/article/pii/001793109190068P>. [Accessed March 2023].
- [72] B. Mondal, C. F. Lopez, A. Verma and P. P. Mukherjee, "Vortex generators for active thermal management in lithium-ion battery systems," in *International Journal of Heat and Mass Transfer*, 2018, pp. 800-815.
- [73] IEC, 61215-1: terrestrial photovoltaic (PV) modules—Design qualification and type approval—Part 1: Test requirements, 2016.
- [74] Z. Zhou, P. Bahl, S. Tkachenko, A. Hari and C. d. Silva, "Vortex Generators for Passive Cooling of Rooftop Photovoltaic Systems Under Free Convection," IEEE, Sydney, 2023.
- [75] [Online]. Available: <https://greentumble.com/do-solar-panels-cause-roof-leaks>.
- [76] [Online]. Available: <https://gienergy.com.au/worlds-largest-solar-farm/>.

## Appendices

### Appendix A

Formations of solar panels



*Figure 57 Rooftop solar array [74]*



*Figure 58 Solar farm array [75]*

## Appendix B

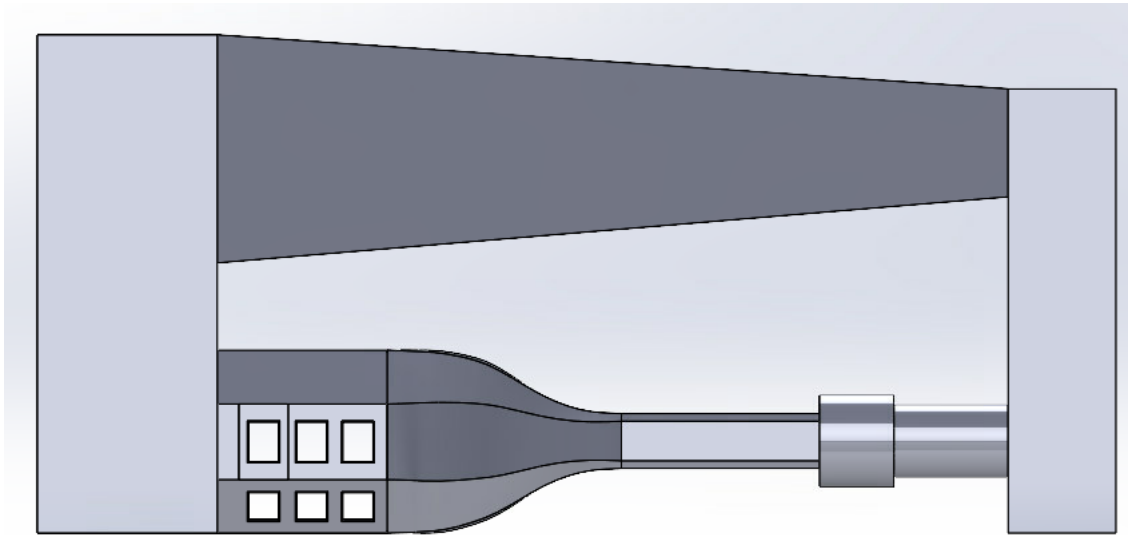


*Figure 59 CAD of LWT*

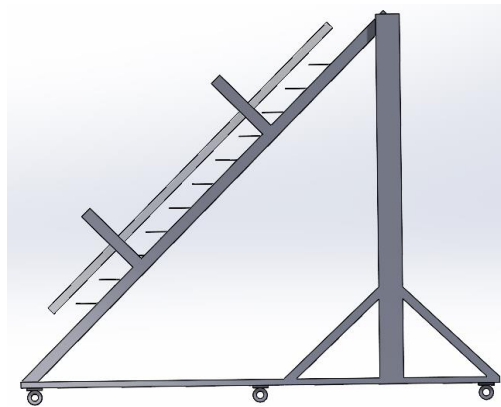


*Figure 60 Forward facing VGs*

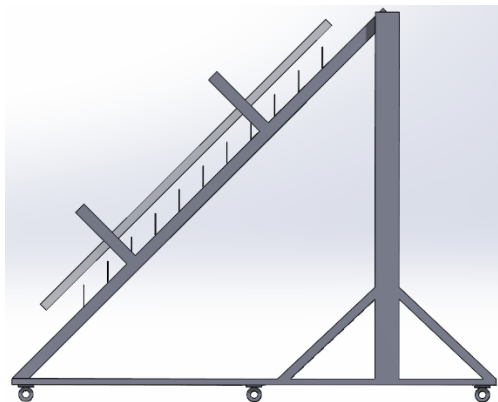


*Figure 61 Backwards facing VGs*



## Appendix C

### Renolds number calculations

Reynolds number formula

$$Re = \frac{\rho u_m D_h}{\mu}$$

Properties at 25°C:

$$\rho = 1.184$$

$$\mu = 1.849 * 10^{-5}$$

$$D_h = \frac{4A_c}{P} = \frac{4(1 \times 0.1)}{2 + 0.2} = 0.1818$$

*Insert a hydraulic diameter fig*

$$Re = \frac{\rho u_m D_h}{\mu}$$

## Appendix D

### MATLAB code

#### Read\_VG\_Data.m

```

%% Load existing data

[fv,pv] = uigetfile({'*.mat'},'Select VG Data');
load([pv,fv])
%% Load IR Data

[fn,pn] = uigetfile({'*.csv'},'Select IR Data (CSV File)');
data = importfile([pn fn]);
params = importparams([pn fn]);
clear fn; clear pn;

%% Rotate Data

if size(data,1) == 464
    data = imrotate(data,-90);
end

%% Find edge and corners of the image

[Gmag, ~] = imgradient(data,'prewitt'); % Gradient of the data (To find edge of the module)
Gmag(Gmag<5) = 0; % Set the low values in gradient to zero (removes noise)

Gmag = im2bw(Gmag); % Binarize the image

% Following 5 lines manipulate data to assist in finding corner coordinates
tp_th = 25; bt_th = 25; % set bottom and top right mask thickness
Gmag(1:60,1:tp_th) = 1; Gmag(250:348,1:bt_th) = 1; % set bottom and top right mask
Gmag(1:39,:) = 1; % TOP region
Gmag(302:348,:) = 1; % BOTTOM region
Gmag(:,437:464) = 1; % RHS region
Gmag(61:250,1:50) = 0;
Gmag(1,:) = 1; Gmag(348,:) = 1;
% %
Gmag = imfill(Gmag,'holes'); %Gmag(:,1:5) = 1; % Fill holes in the data
imagesc(Gmag)
%
Image = imcomplement(Gmag); % Invert the data

%% Find Corners on the distorted data
[I,J]=find(Image>max(Image(:))/2);
IJ=[J,I];
[~,idx]=min(IJ*[1 1; -1 -1; 1 -1; -1 1].');
corners=IJ(idx,:);
corners = corners+[0,0;0,-4;0,-4;0,0]; % compensate for coordinate shift due to bottom edge
reflection

%% Create Transform for dewarping

fixedPoints = [0 0; 590 350; 0 350; 590 0]; % Edge coordinates of dewarped data
movingPoints = corners;
tform = fitgeotrans(movingPoints,fixedPoints, 'projective');
Cal_image = imwarp(Image, tform);
[I,J]=find(Cal_image>max(Cal_image(:))/2);

```

```

IJ=[J,I];
[~,idx]=min(IJ*[1 1; -1 -1; 1 -1; -1 1].');
cal_cor=IJ(idx,:);

%% Dewarp Data
Cal_data = imwarp(data,tform);
Cal_data = imcrop(Cal_data,[(bt_th+8) cal_cor(1,2)-13 619 379]); % [xmin ymin width height].

%% Update data in i row location (VG)
i = size(s_vg,2)+1;
s_vg(i).Emmisivity = str2num(params(1));

Tamb = char(params(4,1));
Tamb = str2double(Tamb(1:4));
if isnan(Tamb) == 1
    Tamb = char(params(4,1));
    Tamb = str2double(Tamb(1:3));
    if isnan(Tamb) == 1
        Tamb = char(params(4,1));
        Tamb = str2double(Tamb(1:2));
    end
end
s_vg(i).T_amb = Tamb;

Tref = char(params(2,1));
Tref = str2double(Tref(1:4));
if isnan(Tref) == 1
    Tref = char(params(2,1));
    Tref = str2double(Tref(1:3));
    if isnan(Tref) == 1
        Tref = char(params(2,1));
        Tref = str2double(Tref(1:2));
    end
end
s_vg(i).T_refl = Tref;
s_vg(i).Vg_Length = 14;
s_vg(i).RH = 50;
s_vg(i).T_optics = 20;
s_vg(i).Py = 12;
s_vg(i).VG_Width = 4;
s_vg(i).Cal_Data=Cal_data;
s_vg(i).IR_data=data;

%% Update Mat Files
save("VG.mat", "s_vg")

```

## Delta\_T.m

```

%% Load Baseline and VG mat files
clc
clear

[fb,pb] = uigetfile({'*.mat'}, 'Select Baseline Data');
load([pb,fb])
[fv,pv] = uigetfile({'*.mat'}, 'Select VG Data');
load([pv,fv])

%% Mean cell temp for middle 2 rows (Baseline)

for i = 1:length(s_b)
    Cal_data = s_b(i).Cal_Data;
    temp = Cal_data(75:300,2:500);
    mean_2(i,:) = mean(temp(65:105,:));
    mean_3(i,:) = mean(temp(120:160,:));
    temp2 = mean_2(i,:);
    temp3 = mean_3(i,:);
    avg_2b(i,:) = [mean(temp2(1:62)) mean(temp2(1*62:2*62)) mean(temp2(2*62:3*62))...
        mean(temp2(3*62:4*62)) mean(temp2(4*62:5*62)) mean(temp2(5*62:6*62)) ...
        mean(temp2(6*62:7*62)) mean(temp2(7*62:8*62))];
    avg_3b(i,:) = [mean(temp3(1:62)) mean(temp3(1*62:2*62)) mean(temp3(2*62:3*62))...
        mean(temp3(3*62:4*62)) mean(temp3(4*62:5*62)) mean(temp3(5*62:6*62)) ...
        mean(temp3(6*62:7*62)) mean(temp3(7*62:8*62))];
    std_2b(i,:) = [std(temp2(1:62)) std(temp2(1*62:2*62)) std(temp2(2*62:3*62))...
        std(temp2(3*62:4*62)) std(temp2(4*62:5*62)) std(temp2(5*62:6*62)) ...
        std(temp2(6*62:7*62)) std(temp2(7*62:8*62))];
    std_3b(i,:) = [std(temp3(1:62)) std(temp3(1*62:2*62)) std(temp3(2*62:3*62))...
        std(temp3(3*62:4*62)) std(temp3(4*62:5*62)) std(temp3(5*62:6*62)) ...
        std(temp3(6*62:7*62)) std(temp3(7*62:8*62))];
end
clear mean_1; clear mean_2; clear mean_3; clear mean_4; clear temp; clear temp2; clear temp3;
clear Cal_data;

%% Mean cell temp for middle 2 rows (Vg)

for i = 1:length(s_vg)
    Cal_data = s_vg(i).Cal_Data;
    temp = Cal_data(75:300,2:500);
    mean_2(i,:) = mean(temp(65:105,:));
    mean_3(i,:) = mean(temp(120:160,:));
    temp2 = mean_2(i,:);
    temp3 = mean_3(i,:);
    avg_2v(i,:) = [mean(temp2(1:62)) mean(temp2(1*62:2*62)) mean(temp2(2*62:3*62))...
        mean(temp2(3*62:4*62)) mean(temp2(4*62:5*62)) mean(temp2(5*62:6*62)) ...
        mean(temp2(6*62:7*62)) mean(temp2(7*62:8*62))];
    avg_3v(i,:) = [mean(temp3(1:62)) mean(temp3(1*62:2*62)) mean(temp3(2*62:3*62))...
        mean(temp3(3*62:4*62)) mean(temp3(4*62:5*62)) mean(temp3(5*62:6*62)) ...
        mean(temp3(6*62:7*62)) mean(temp3(7*62:8*62))];
    std_2v(i,:) = [std(temp2(1:62)) std(temp2(1*62:2*62)) std(temp2(2*62:3*62))...
        std(temp2(3*62:4*62)) std(temp2(4*62:5*62)) std(temp2(5*62:6*62)) ...
        std(temp2(6*62:7*62)) std(temp2(7*62:8*62))];
    std_3v(i,:) = [std(temp3(1:62)) std(temp3(1*62:2*62)) std(temp3(2*62:3*62))...
        std(temp3(3*62:4*62)) std(temp3(4*62:5*62)) std(temp3(5*62:6*62)) ...
        std(temp3(6*62:7*62)) std(temp3(7*62:8*62))];
end
clear mean_1; clear mean_2; clear mean_3; clear mean_4; clear temp; clear temp2; clear temp3;
clear Cal_data;

```

```

%% Mean temperature of middle rows

% Baseline
for i = 1:size(avg_2b,1)
    avg_row(:,i) = mean([avg_2b(i,:) avg_3b(i,:)']');
    s_b(i).Mean_cell = avg_row(:,i);
end

% Vg
for i = 1:size(avg_2v,1)
    avg_row_vg(:,i) = mean([avg_2v(i,:) avg_3v(i,:)']');
    s_vg(i).Mean_cell = avg_row_vg(:,i);
end

clear avg_row; clear avg_row_vg;
%%
% makes it easier to handle data
baseline_table = struct2table(s_b);
s_vg_table = struct2table(s_vg);

% reshapes it into a nice table
meancellbase = cell2mat(baseline_table.Mean_cell);
meancellbase = reshape(meancellbase, 8, []); % 63x8 table of Mean_cell from b

% meancellvg = cell2mat(s_vg_table.Mean_cell);
% meancellvg = reshape(meancellvg, 8, []); % 90x8 table of Mean_cell from vg

% this finds the location of where speed = 1/2/3 in the baselines
b1 = find(baseline_table.speed < 2);
b2 = find(baseline_table.speed >= 2 & baseline_table.speed < 3);
b3 = find(baseline_table.speed >= 3);

% this finds the location of where speed = 1/2/3 in the VG cases
vg1 = find(s_vg_table.speed < 2);
vg2 = find(s_vg_table.speed >= 2 & s_vg_table.speed < 3);
vg3 = find(s_vg_table.speed >= 3);

c = 1:8; % creating vals for rows in module 1-8

%%
% this creates relationships between amb temp (b) and each col of baseline
% mean_cell for speed = 1ms
X1 = cell(1,8);
for j = c
    X1{j} = fit(baseline_table.T_refl(b1), meancellbase(b1, j), 'poly1');
end

% for speed = 2ms
X2 = cell(1,8);
for j = c
    X2{j} = fit(baseline_table.T_refl(b2), meancellbase(b2, j), 'poly1');
end

% for speed = 2ms
X3 = cell(1,8);
for j = c
    X3{j} = fit(baseline_table.T_refl(b3), meancellbase(b3, j), 'poly1');
end

```

```

%%
% make T_pred 8 cells accurate using this process

% 1ms
for j = vg1
    for i = c
        T_pred(j,i) = X1{1,i}(s_vg_table.T_refl(j));
    end
end

% letmeknow = mean(T_pred(1,:)); % check that the 8 cells averages
% to OG T_pred = 53.7774 -- it works, yay

% 2ms
for j = vg2
    for i = c
        T_pred(j,i) = X2{1,i}(s_vg_table.T_refl(j));
    end
end

% 3ms
for j = vg3
    for i = c
        T_pred(j,i) = X3{1,i}(s_vg_table.T_refl(j));
    end
end

s_vg_table.T_pred = T_pred;

s_vg = table2struct(s_vg_table);

%% Delta T

% USE THIS METHOD
for i = 1:length(s_vg)
    del_T(i,:) = -(s_vg(i).Mean_cell-s_vg(i).T_pred');
    s_vg(i).delta_T = del_T(i,:);
    s_vg(i).mean_delta_T = mean(s_vg(i).delta_T(1:8));
end
%
% % TRIAL svetlana method
% for i = 1:length(s_vg)
%     mean_VG(i) = mean(s_vg(i).Mean_cell(2:8));
%     mean_pred(i) = mean(s_vg(i).T_pred(2:8));
%     delT = (mean_pred - mean_VG)';
%     s_vg(i).mean_delta_T = delT(i);
% end

%% Save updated Mat files

% save([pb, 'Baseline_final1.mat'], 's_b')
% save([pv, 'VG_final1.mat'.mat'], 's_vg')

%%
%
figure(1)
hold on
for i = b1
    B = meancellbase(i,2:8); % change 2 to 1

```

```

    scatter(c, B)
end
hold off
%
%% plot the fit case curves
% for 8 cells

FontName = 'Times New Roman';
FontSize = 12;
Linewidth = 1.2;
figure()
set(gcf, 'color', 'w');
hold on
% this is for plotting row 1
% for i = b1
%     A = baseline_table.T_refl(i);
%     B = meancellbase(i,1);
%     scatter(A, B)
% end

xlim([0 35])
ylim([20 60])

plot(X1{1,1}, 'b')
plot(X1{1,2}, 'g')
plot(X1{1,3}, 'k')
plot(X1{1,4}, 'y')
plot(X1{1,5}, 'r')
plot(X1{1,6}, '--')
plot(X1{1,7}, 'c')
plot(X1{1,8}, 'm')
hold off

xlabel('T_{amb} ^\circ C', 'FontSize', FontSize, 'FontWeight', 'normal', 'FontName',
FontName);
ylabel('T_{module}', 'FontSize', FontSize, 'FontWeight', 'normal', 'FontName', FontName);
legend({'Row1', 'Row2', 'Row3', 'Row4', 'Row5', 'Row6', 'Row7', 'Row8'})

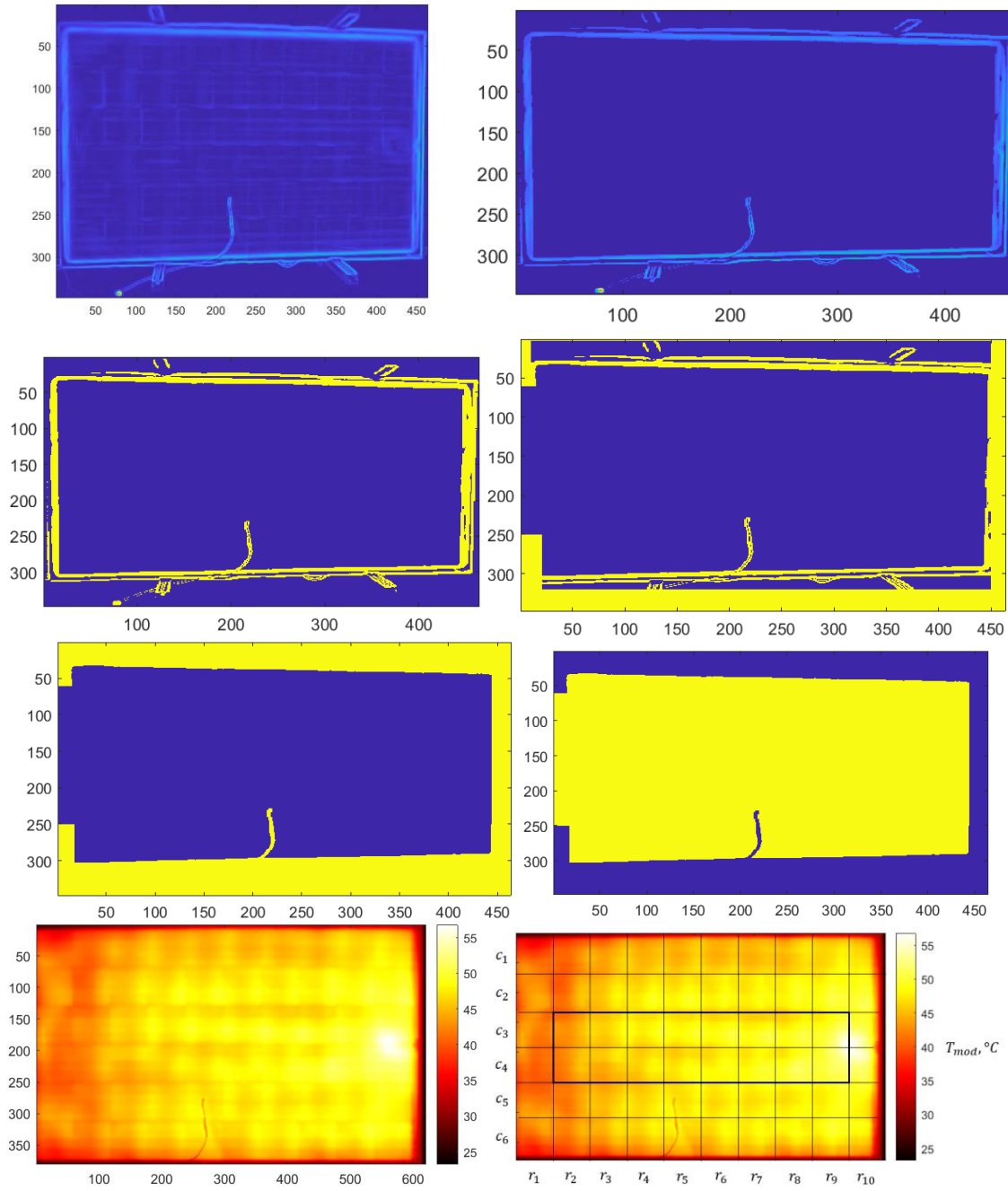
set(gca, 'Layer', 'top', 'TickLabelInterpreter', 'none', 'FontSize', FontSize, 'FontName', FontName,
'box', 'on', 'LineWidth', ...

1, 'FontWeight', 'normal', 'XColor', 'k', 'YColor', 'k', 'ZColor', 'k', 'LabelFontSizeMultiplier', 1, 'Units', 'inches', 'Position', [1 1 3.5 2]);

% give the Figures names as you export them
% exportgraphics(gcf, 'delT_graphically.png', 'Resolution', 600);

```

Figures of module cropping to size throughout the coding process





## Appendix E

VG Case	Speed	Sample Size	Mean	Median	STD	STD (STD)
Fwd_full_SP	1	10	1.272	0.7531	0.9331	0.1014
	2	10	0.4072	-0.092	0.7474	
	3	10	0.0125	-0.537	0.9108	
Fwd_half_SP	1	3	1.0483	1.0717	0.0763	0.0485
	2	3	0.6822	0.7034	0.0499	
	3	3	0.5486	0.5738	0.1439	
Back_full_SP	1	5	1.4554	1.4647	0.2538	0.1030
	2	5	0.7422	0.7633	0.0772	
	3	5	0.7028	0.7258	0.0736	
Back_half_SP	1	3	0.3324	0.2816	0.2021	0.1235
	2	3	-0.098	0.1451	0.4298	
	3	3	-0.1272	0.0725	0.3991	
Fwdback_full_SP	1	5	1.81979	1.9047	0.2257	0.1127
	2	5	1.03854	1.0388	0.0408	
	3	5	1.007	0.9973	0.0217	